Auxetic anti-tetrachiral materials: equivalent elastic properties and frequency band-gaps

Andrea Bacigalupo [1] and Maria Laura De Bellis [2]

[1] *IMT Institute for Advanced Studies Lucca, Piazza San Francesco, 19, 55100, Lucca, Italy*

[2] *Dipartimento di Ingegneria Civile ed Ambientale, Politecnico di Milano,*
Piazza Leonardo da Vinci, 32, 20133 Milano, Italy

Abstract

A comprehensive characterization of the novel class of anti-tetrachiral cellular solids, both considering the static and the dynamic response, is provided in the paper.

The heterogeneous material is characterized by a periodic microstructure made of equi-spaced rings each interconnected by four ligaments. In the most general case, rings and ligaments are surrounded by a softer matrix and the rings can be filled by a different material.

First, the first order linear elastic homogenized constitutive response is estimated resorting to two different microstructural models: a discrete model, in which the ligaments are modeled as beams and the presence of the matrix is neglected and the equivalent elastic properties are evaluated through a simplified analytical approach, and a more detailed continuous model, where the actual properties of matrix, ligaments and rings, varying in the 2D domain, are considered and the first order computational homogenization is adopted. Special attention is given to the dependence of the 2D overall Cauchy-type elastic constants on the mechanical and geometrical parameters characterizing the microstructure. The results, indeed, show the existence of large variations in the linear elastic constants and degree of anisotropy. A comparison with available experimental results confirms the validity of the analytical and numerical approaches adopted.

Finally, the rigorous Floquet-Bloch approach is applied to the Periodic Cell of the cellular solid to evaluate the dispersion of propagation waves along the orthotropic axes in the framework of elasticity and to detect band gaps characterizing the material. A numerical approach, based on the first order computational homogenization, is also adopted and the rigorous and approximate solutions are compared.

Email address: [1] `andrea.bacigalupo@imtlucca.it`,[2] `marialaura.debellis@polimi.it` (Andrea Bacigalupo [1] and Maria Laura De Bellis [2])

1. Introduction

Auxetic materials exhibit peculiar properties related to a zero or negative Poisson's ratio: they expand laterally when subjected to stretching and contract laterally when compressed, as explained in (Lakes, 1987, 1991; Prawoto, 2012; Sigmund et al., 1998). This unusual behavior is mostly obtained in man-made materials (Greaves et al., 2011), even though it is possible to find in nature some auxetic materials.

Examples are cellular materials, honeycomb structures and networks (Smith et al., 2000), sandwich core materials adopted in marine, automotive and aerospace lightweight structures (Alderson et al., 2010), as well as origami structures (Schenk and Guest, 2013). The main advantages observed are related to an increase of the shear modulus, fracture toughness (due to an increase of the energy absorption under static and dynamic loading), high acoustic damping and indentation resistance, as reported in (Lakes, 1993; Dirrenberger et al., 2013).

Focusing on periodic cellular lattice structures (Cadman et al., 2013), different topologies can be described. Among others, the chiral topology, (Prall and Lakes, 1996), is typical of periodic honeycomb structures made of rings inter-connected by tangent straight ligaments. In this case, the overall auxetic behavior is obtained thanks to a special deformation mechanism characterized by winding ligaments onto the nodes: when an in-plane stress is applied, the ligaments remain tangent to the nodes and a change of area without change of shape is observed.

Recent studies (Gaspar et al., 2005; Scarpa et al., 2007; Grima et al., 2008; Dos Reis and Ganghoffer, 2012; Chen et al., 2013; Gatt et al., 2013; Ma et al., 2013; Cauchi and Grima, 2014) pointed out that the out-of-plane stiffness properties can be regulated by varying the internal geometry, i.e. the relative position between nodes and the number and position of ligaments. Trichiral, tetrachiral and hexachiral honeycombs (Alderson et al., 2010), are examples of different chiral tessellations which owe their name to the number of ligaments (3,4 and 6, respectively) tangentially attached to each ring.

Also "anti-chiral" systems have been designed in which the same side of the ligaments is connected to adjacent ring, so that the nearest-neighboring rings are characterized by opposite chirality.

The paper by (Prall and Lakes, 1996) marked the beginning of the study of the mechanical response of hexachiral structures in the framework of linear elasticity. Subsequent developments involved the

2

analysis of damage processes (Bettini et al., 2010), and of free wave propagation (Spadoni et al., 2009). Furthermore, the phononic properties of the tetrachiral and anti-tetrachiral periodic cell were investigated by (Tee et al., 2010; Ma et al., 2013) who adopted the Floquet-Bloch approach via a FE analysis. A very interesting property of cellular lattice structures is, indeed, the capability of acting as filters, attenuating elastic waves over certain frequency bands.

Noteworthy is also the contribution by (Dirrenberger et al., 2011, 2013) in the analysis of the overall elastic properties of chiral and anti-chiral cellular solids. The classical homogenization approach is adopted, through a finite element discretization of the periodic cell. This approach has been extended by (Dirrenberger et al., 2012), to the analysis of the elasto-plastic response of hexachiral ductile materials.

Recently, (Bacigalupo and Gambarotta, 2014a) performed the homogenization of auxetic cellular solids, having periodic hexachiral and tetrachiral microstructure, by means of two different techniques. The first approach is based on the representation of the cellular solid as a beam-lattice homogenized as a micropolar continuum. The second approach is developed to analyze periodic cells conceived as a two-dimensional domain consisting of deformable portions such as the ring, the ligaments and a possibly embedded matrix. It results that the beam-lattice models are able to describe in detail the dependence of the elastic overall moduli on the geometry of the microstructure and on the length of the ligaments. Nevertheless, these models provide accurate results only for very slender ligaments, a circumstance that does not seem to occur in samples commonly used in experiments where the effective length of the ligament is not easy to identify. Furthermore, this model neglects the presence of the material filling the gaps between the ligaments and within the rings. The choice of an equivalent local or non-local continuum model at the macroscale (based on a FE description of the periodic cell) turns out, therefore, to be the most adequate.

Various approaches are available in literature for the homogenization of periodic composite materials. The global response of the homogenized material can be obtained via computational or asymptotic homogenization techniques resorting to different continuum models, both classical (Miehe, 2002) and enhanced, i.e. Cosserat (Forest and Sab, 1998; Forest, 2002; Trovalusci et al., 2009; De Bellis and Addessi, 2011; Addessi et al., 2013) or second order (Kouznetsova et al., 2004; Bacigalupo and Gambarotta, 2010, 2013; Bacca et al., 2013a,b; Bacigalupo, 2014). The advantages of adopting an enhanced continuum model are mainly due to the presence of length scale parameters in the constitutive structure.

This paper is devoted to the study of a special type of chiral cellular solids, very promising for prac-

3

tical applications, i.e. the so-called anti-tetrachiral, which differs from tetrachiral for the position of the ligaments. A schematic of the internal arrangement is shown in Figure 1. In the most general case the ligaments are surrounded by a softer matrix. It is, also, assumed that the rings are made of the same material of ligaments and may be filled with a different material. Experimental results performed by (Alderson et al., 2010) showed that the anti-tetrachiral cellular solids exhibit pronounced anisotropic behavior and a strong chirality, i.e. Poisson's coefficients close to -1.

At the moment an in-depth characterization of this type of cellular solid is still lacking and a parametric study, aimed to describe both the static and the dynamic responses, can be a useful tool to design the microstructure with tuned global properties.

The aim of this work is, therefore, to provide a complete characterization of the response of this
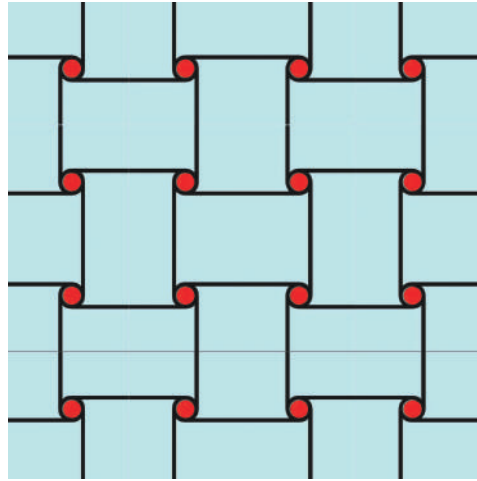

Figure 1: Schematic of anti-tetrachiral cellular material. Each equi-spaced ring is connected by four ligaments and can be filled by a material (in red) different from the matrix (in light blue).

novel class of cellular solids, both involving the estimation of the equivalent elastic properties and the detection of possible band-gaps.

Initially, the first order linear elastic homogenized constitutive response is estimated adopting two different models for the description of the microscopic level: a discrete beam network model, i.e. a simplified approach in which the ligaments are modeled as beams and the presence of the matrix is neglected, and a continuous model, where the actual properties of matrix, ligaments and rings, varying in the 2D domain, are reproduced in detail. Special attention is given to the dependence of the 2D overall Cauchy-type elastic constants on the mechanical and geometrical parameters, characterizing the microstructure. The results, indeed, show the existence of large variations in linear elastic constants and degree of anisotropy. This is a key aspect to design materials with tailored properties.

4

The second part of the work focuses on the 2D elasto-dynamic dispersion analysis adopting the Floquet-Bloch decomposition.

A Floquet-Bloch wave approach is, thus, applied to the periodic cell of the cellular solid to evaluate the properties of the dispersion functions of waves propagating in different directions and to detect band gaps characterizing the material as the mechanical parameters of the periodic cell vary (in terms of ratio between Young's moduli). The dispersive waves in anti-tetrachiral cellular solids are analyzed along the orthotropic axes.

The paper is organized as follows: in Section 2 the geometry of the periodic anti-tetrachiral lattice is briefly described; in Section 3 the static modeling is addressed by resorting to two different microstructural models: the beam lattice model 3.1 and the first order continuous model 3.2. The numerical results and the comparison between the different approaches are reported in 3.3 and it is emphasized that, despite the strong simplifying assumptions of the beam lattice model, this approach gives reasonable results, comparable with those of the richer model, at least when the matrix is neglected. In Section 4 the dynamic properties of the anti-tetrachiral lattice are studied. A further numerical investigation is performed on the flexural wave propagation properties. A Floquet–Bloch approach is applied to the periodic cell and the dispersion functions for waves along the orthotropic axes are evaluated as the ratio between Young's moduli of the constituents vary. Finally, in Section 5 some concluding remarks are reported.

2. Anti-tetrachiral cellular solid

The geometry of the periodic cell is schematically reported in Figure 2. Four rings of radius R are centered at the corners of an ideal square of side L and are interconnected by tangent ligaments. Rings and ligaments have the same width t and are possibly filled with a soft matrix. Linear elastic isotropic behavior is assumed for all the constituents.

In the following, a generic microscopic material point $\mathbf{x} = x_1\mathbf{e}_1 + x_2\mathbf{e}_2$ is referred to a system of coordinates with origin at point O and orthogonal base $(\mathbf{e}_1, \mathbf{e}_2)$. The macroscopic material point is referred to as $\mathbf{X} = \{X_1 \ X_2\}^T$ and the periodic cell is selected such that $\mathbf{X} = \mathbf{0}$ coincides with its geometric center.

3. Linear elastic homogenized properties evaluation

Consistently with the well established homogenization approaches, two scales of interest are considered: a macro-scale, the structural one, in which the material is studied as a homogenized medium
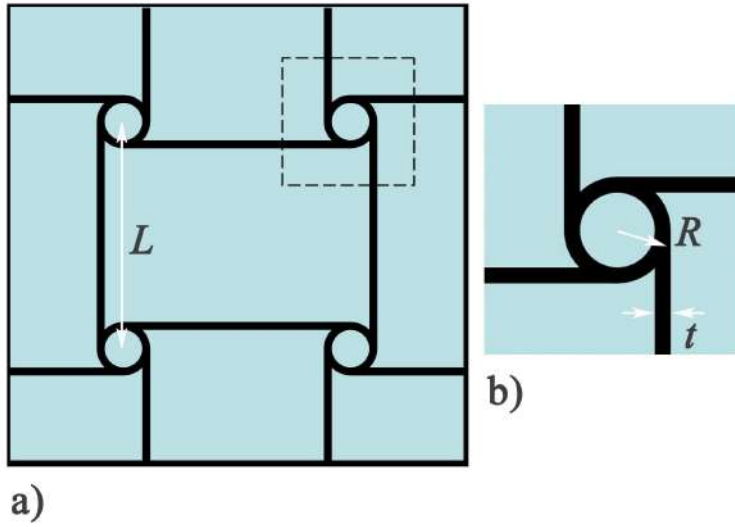
Figure 2: Geometry of the anti-tetrachiral cellular solid: a) periodic cell; b) detail of one ring and the attached ligaments.

and a micro-scale where all the information regarding the mechanical and geometric properties of the constituents are described in detail.

In what follows the alternative models adopted at the microscopic level to estimate the first order homogenized linear elastic constitutive response of anti-tetrachiral cellular solids are presented and discussed in Sections 3.1 and 3.2.

3.1. Discrete model: periodic beam network

A discrete model is considered, where the ligaments are modeled as elastic Euler-Bernoulli beams undergoing small deformations and interconnected by perfectly rigid nodes, i.e. rings filled by the same material, as in (Alderson et al., 2010; Scarpa et al., 2007; Chen et al., 2013). No matrix, filling the rings and the gaps between ligaments, is taken into account in this approximation.

Consistently with the homogenization techniques, it is assumed that the homogenized first order constitutive response of the beam network can be obtained by solving a properly defined Boundary Value Problem (BVP) on a single Periodic Cell, representative of the anti-tetrachiral cellular solid and undergoing periodic boundary conditions.

In Figure 3 a schematic of the Periodic Cell is reported. The periodic portion consists of four beams of length L and eight beams of length $L/2$ connected by four rigid elements arranged in a cross-configuration reproducing the effect of the rigid rings (the length of each arm of the cross is R). The system, therefore, includes twelve nodes, each characterized by two translational degrees of freedom

6

u_1, u_2 aligned with the global horizontal and vertical directions, respectively, and a rotational degree of freedom, ϕ. Periodicity conditions hold between corresponding nodes on the edges of the Periodic
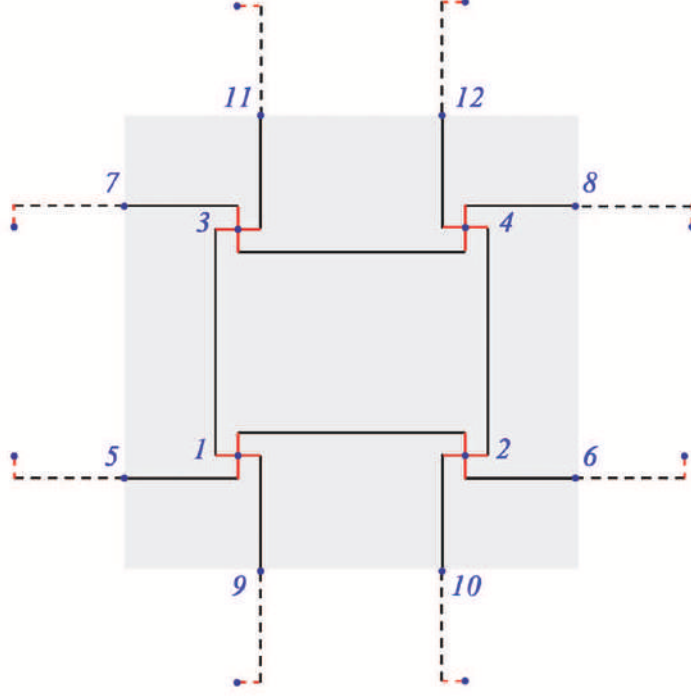

Figure 3: Schematic of the periodic cell adopted in the beam lattice model. Four internal and eight external nodes are considered. Dashed portions of the beams are not included in the cell.

Cell (5-6; 7-8; 9-11; 10-12).

A one to one correspondence is established between a macroscopic point $\mathbf{X} = \{X_1, X_2\}^T$ of the first order homogenized continuum, characterized by the displacement components $U_1(\mathbf{X})$ and $U_2(\mathbf{X})$, and the Periodic Cell, that is a portion of the actual material, referred as the microscopic level.

At the microscopic level, the translational components of the displacement field of a point P of the beam network can be expressed by means of the following standard additive decomposition into assigned terms $u_i^*(\mathbf{X}, \mathbf{x})$ (i=1,2), depending on macroscopic parameters, and unknown perturbation terms $\tilde{u}_i(\mathbf{X}, \mathbf{x})$ (i=1,2) related to the local solution of the BVP, as:

$$u_i(\mathbf{X}, \mathbf{x}) \;=\; u_i^*(\mathbf{X}, \mathbf{x}) + \tilde{u}_i(\mathbf{X}, \mathbf{x}) \quad \text{with} \quad i = 1, 2 \tag{1}$$

where the dual dependence on the macroscopic $\mathbf{X}$ and the microscopic $\mathbf{x}$ coordinates is explicitly stated.

In Eq. (1), $u_i^*(\mathbf{X}, \mathbf{x})$ are linear polynomial functions depending on the macro-displacement $U_i(\mathbf{X})$ and macro-strain components $E_{ij}(\mathbf{X})$, as:

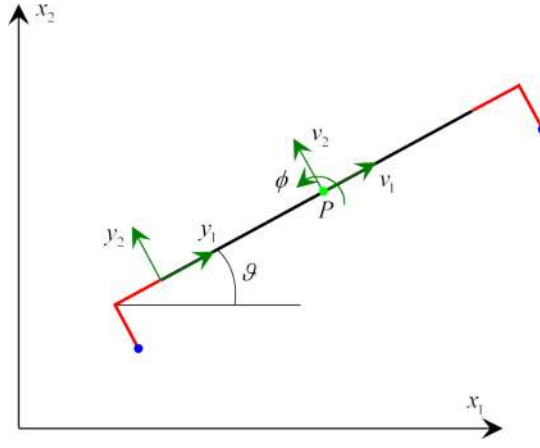$$u_i^*(\mathbf{X}, \mathbf{x}) \;=\; U_i(\mathbf{X}) + E_{ij}(\mathbf{X})x_j \quad \text{with} \quad i, j = 1, 2 \tag{2}$$

7

Figure 4: Generic beam element endowed with local reference frame.

where $E_{ij} = sym(\partial U_i / \partial X_j)$, and the symbol $sym(\cdot)$ represents the symmetric part of $(\cdot)$.

The perturbation terms $\tilde{u}_i(\mathbf{X}, \mathbf{x})$ are obtained as:

$$\tilde{u}_i(\mathbf{X}, \mathbf{x}) = \Lambda^1_{ipq}(\mathbf{x}) E_{pq}(\mathbf{X}) \tag{3}$$

with $\Lambda^1_{ipq}(\mathbf{x})$ being perturbation functions, solution of the BVP with periodic boundary conditions. In Figure 4 a generic beam is reported endowed with a local reference frame $\mathbf{y} = \{y_1, y_2\}$, aligned with the beam axis. The local displacement degrees of freedom are defined as $v_1(\mathbf{X}, \mathbf{x})$, $v_2(\mathbf{X}, \mathbf{x})$ and $\phi(\mathbf{X}, \mathbf{x})$. The portions of the rigid crosses pertaining to the considered beam are drawn in red. The rotation of a generic point can be expressed with respect to the local displacement components as:

$$\phi(\mathbf{X}, \mathbf{x}) = \frac{\partial v_2(\mathbf{X}, \mathbf{x})}{\partial y_1} \tag{4}$$

while with respect to the global displacement components it is defined as:

$$\phi(\mathbf{X}, \mathbf{x}) = Q_{2j} Q_{1p} \frac{\partial u_j(\mathbf{X}, \mathbf{x})}{\partial x_p} \tag{5}$$

where the rotation tensor $\mathbf{Q}$ is:

$$\mathbf{Q}(\vartheta) = \begin{bmatrix} cos\vartheta & sin\vartheta \\ -sin\vartheta & cos\vartheta \end{bmatrix} \tag{6}$$

ϑ being the angle shown in Figure 4.

Also the ϕ component can be split into an assigned and a perturbation term:

$$\phi^*(\mathbf{X}, \mathbf{x}) = Q_{2j} Q_{1p} \delta_{jt} \delta_{pq} E_{tq}(\mathbf{X}) \tag{7}$$

and

$$\tilde{\phi}(\mathbf{X}, \mathbf{x}) = Q_{2j} Q_{1p} \frac{\partial \Lambda^1_{jtq}(\mathbf{x})}{\partial x_p} E_{tq}(\mathbf{X}) \tag{8}$$

8

The discrete system of beams can be solved resorting to the displacement method and the main steps are described below. Rigid-end offset, modeling the cross rigid elements, are considered. For the sake of brevity, in what follows the explicit dependence of functions on $\mathbf{X}$ and $\mathbf{x}$ will be omitted. The basic relations for the beam system ranging from the definition of the degrees of freedom of the generic beam nodes until the determination of the element stiffness matrix and the vector of nodal forces are reported in Appendix A.

The assembling procedure of the global stiffness matrix $\mathbf{K}$ and nodal force vector $\mathbf{b}$ is, thus, performed and the global system of governing equations in compact form results as:

$$\mathbf{K}\mathbf{w} = \mathbf{b} \tag{9}$$

where $\mathbf{w}$ is the vector collecting the displacements u_1, u_2 and the rotation ϕ of all the nodes of the beam network. By making explicit a distinction between internal I and external E nodes (I are nodes 1-2-3-4 and E are 5-6-7-8-9-10-11-12 in Figure 3), the system in Eq.(9) becomes:

$$\begin{bmatrix} \mathbf{K}_{II} & \mathbf{K}_{IE} \\ \mathbf{K}_{EI} & \mathbf{K}_{EE} \end{bmatrix} \begin{Bmatrix} \mathbf{w}_I \\ \mathbf{w}_E \end{Bmatrix} = \begin{Bmatrix} \mathbf{b}_I \\ \mathbf{b}_E \end{Bmatrix} \tag{10}$$

where it is assumed that no external forces acting on the internal nodes arise, i.e. $\mathbf{b}_I = \mathbf{0}$. By applying the static condensation method, the system in (10) can be expressed as a function of only the degrees of freedom relative to the external nodes and it results:

$$\widetilde{\mathbf{K}}\mathbf{w}_E = \mathbf{b}_E \qquad \text{with} \qquad \widetilde{\mathbf{K}} = \left(\mathbf{K}_{EE} - \mathbf{K}_{EI}\mathbf{K}_{II}^{-1}\mathbf{K}_{IE} \right) \tag{11}$$

According to Figure 3, the external boundary of the periodic cell can be divided into the edges parallel to axis x_1 and x_2 defined as Γ_1 and Γ_2, respectively.

Kinematic and static periodic boundary conditions arise between corresponding pairs of points on the edges Γ_1^- (nodes 9-10) and Γ_1^+ (nodes 11-12), and Γ_2^- (nodes 5-7) and Γ_2^+ (nodes 6-8). The Eqq. (11) can be, thus, rewritten as:

$$\begin{bmatrix} \widetilde{\mathbf{K}}_{\Gamma_1^+\Gamma_1^+} & \widetilde{\mathbf{K}}_{\Gamma_1^+\Gamma_1^-} & \widetilde{\mathbf{K}}_{\Gamma_1^+\Gamma_2^+} & \widetilde{\mathbf{K}}_{\Gamma_1^+\Gamma_2^-} \\ \widetilde{\mathbf{K}}_{\Gamma_1^-\Gamma_1^+} & \widetilde{\mathbf{K}}_{\Gamma_1^-\Gamma_1^-} & \widetilde{\mathbf{K}}_{\Gamma_1^-\Gamma_2^+} & \widetilde{\mathbf{K}}_{\Gamma_1^-\Gamma_2^-} \\ \widetilde{\mathbf{K}}_{\Gamma_2^+\Gamma_1^+} & \widetilde{\mathbf{K}}_{\Gamma_2^+\Gamma_1^-} & \widetilde{\mathbf{K}}_{\Gamma_2^+\Gamma_2^+} & \widetilde{\mathbf{K}}_{\Gamma_2^+\Gamma_2^-} \\ \widetilde{\mathbf{K}}_{\Gamma_2^-\Gamma_1^+} & \widetilde{\mathbf{K}}_{\Gamma_2^-\Gamma_1^-} & \widetilde{\mathbf{K}}_{\Gamma_2^-\Gamma_2^+} & \widetilde{\mathbf{K}}_{\Gamma_2^-\Gamma_2^-} \end{bmatrix} \begin{Bmatrix} \mathbf{w}_E^{\Gamma_1^+} \\ \mathbf{w}_E^{\Gamma_1^-} \\ \mathbf{w}_E^{\Gamma_2^+} \\ \mathbf{w}_E^{\Gamma_2^-} \end{Bmatrix} = \begin{Bmatrix} \mathbf{b}_E^{\Gamma_1^+} \\ \mathbf{b}_E^{\Gamma_1^-} \\ \mathbf{b}_E^{\Gamma_2^+} \\ \mathbf{b}_E^{\Gamma_2^-} \end{Bmatrix} \tag{12}$$

and the kinematic and static periodic boundary conditions are defined according to the following relations between corresponding pairs of points on the edges:

9

- Kinematic BCS:

$$\mathbf{w}_E^{\Gamma_1^+} - \mathbf{w}_E^{\Gamma_1^-} = \boldsymbol{\Delta}_1$$
$$\mathbf{w}_E^{\Gamma_2^+} - \mathbf{w}_E^{\Gamma_2^-} = \boldsymbol{\Delta}_2$$

(13)

with

$$\boldsymbol{\Delta}_1 = \left\{ \begin{array}{c} E_{11}d_1 \\ E_{21}d_1 \\ 0 \\ E_{11}d_1 \\ E_{21}d_1 \\ 0 \end{array} \right\} \quad \text{and} \quad \boldsymbol{\Delta}_2 = \left\{ \begin{array}{c} E_{12}d_2 \\ E_{22}d_2 \\ 0 \\ E_{12}d_2 \\ E_{22}d_2 \\ 0 \end{array} \right\}$$

(14)

- Static BCS:

$$\mathbf{b}_E^{\Gamma_1^+} + \mathbf{b}_E^{\Gamma_1^-} = \mathbf{0}$$
$$\mathbf{b}_E^{\Gamma_2^+} + \mathbf{b}_E^{\Gamma_2^-} = \mathbf{0}$$

(15)

By substituting the kinematic and static boundary conditions into Eq. (12), in compact form it results:

$$\begin{bmatrix} \mathbf{I} & -\mathbf{I} & \mathbf{0} & \mathbf{0} \\ \mathbf{0} & \mathbf{0} & \mathbf{I} & -\mathbf{I} \\ \mathbf{A}_1 & \mathbf{A}_2 & \mathbf{A}_3 & \mathbf{A}_4 \\ \mathbf{A}_5 & \mathbf{A}_6 & \mathbf{A}_7 & \mathbf{A}_8 \end{bmatrix} \left\{ \begin{array}{c} \mathbf{w}_E^{\Gamma_1^+} \\ \mathbf{w}_E^{\Gamma_1^-} \\ \mathbf{w}_E^{\Gamma_2^+} \\ \mathbf{w}_E^{\Gamma_2^-} \end{array} \right\} = \left\{ \begin{array}{c} \boldsymbol{\Delta}_1 \\ \boldsymbol{\Delta}_2 \\ 0 \\ 0 \end{array} \right\}$$

(16)

where $\mathbf{I}$ and $\mathbf{0}$ are 6×6 identity and zero matrices, respectively; the other submatrices are defined as: $\mathbf{A}_1 = \left(\widetilde{\mathbf{K}}_{\Gamma_1^+\Gamma_1^+} - \widetilde{\mathbf{K}}_{\Gamma_1^-\Gamma_1^+} \right)$, $\mathbf{A}_2 = \left(\widetilde{\mathbf{K}}_{\Gamma_1^+\Gamma_1^-} - \widetilde{\mathbf{K}}_{\Gamma_1^-\Gamma_1^-} \right)$,
$\mathbf{A}_3 = \left(\widetilde{\mathbf{K}}_{\Gamma_1^+\Gamma_2^+} - \widetilde{\mathbf{K}}_{\Gamma_1^-\Gamma_2^+} \right)$, $\mathbf{A}_4 = \left(\widetilde{\mathbf{K}}_{\Gamma_1^+\Gamma_2^-} - \widetilde{\mathbf{K}}_{\Gamma_1^-\Gamma_2^-} \right)$, $\mathbf{A}_5 = \left(\widetilde{\mathbf{K}}_{\Gamma_2^+\Gamma_1^+} - \widetilde{\mathbf{K}}_{\Gamma_2^-\Gamma_1^+} \right)$, $\mathbf{A}_6 = \left(\widetilde{\mathbf{K}}_{\Gamma_2^+\Gamma_1^-} - \widetilde{\mathbf{K}}_{\Gamma_2^-\Gamma_1^-} \right)$,
$\mathbf{A}_7 = \left(\widetilde{\mathbf{K}}_{\Gamma_2^+\Gamma_2^+} - \widetilde{\mathbf{K}}_{\Gamma_2^-\Gamma_2^+} \right)$, $\mathbf{A}_8 = \left(\widetilde{\mathbf{K}}_{\Gamma_2^+\Gamma_2^-} - \widetilde{\mathbf{K}}_{\Gamma_2^-\Gamma_2^-} \right)$. With straightforward manipulations of the last two equations in (16), it is possible to express the displacements $\mathbf{w}_E^{\Gamma_1^-}$ and $\mathbf{w}_E^{\Gamma_2^-}$ in terms of $\mathbf{w}_E^{\Gamma_1^+}$ and $\mathbf{w}_E^{\Gamma_2^+}$ as:

$$\mathbf{w}_E^{\Gamma_1^-} = \mathbf{R}_{\Gamma_1^-\Gamma_1^+} \mathbf{w}_E^{\Gamma_1^+} + \mathbf{R}_{\Gamma_1^-\Gamma_2^+} \mathbf{w}_E^{\Gamma_2^+}$$
$$\mathbf{w}_E^{\Gamma_2^-} = \mathbf{R}_{\Gamma_2^-\Gamma_1^+} \mathbf{w}_E^{\Gamma_1^+} + \mathbf{R}_{\Gamma_2^-\Gamma_2^+} \mathbf{w}_E^{\Gamma_2^+}$$

(17)

where the matrices are $\mathbf{R}_{\Gamma_1^-\Gamma_1^+} = \mathbf{A}_2^{-1} \left[\mathbf{A}_4 \left(\mathbf{A}_8 - \mathbf{A}_5\mathbf{A}_2^{-1}\mathbf{A}_4 \right)^{-1} \left(\mathbf{A}_5 - \mathbf{A}_5\mathbf{A}_2^{-1}\mathbf{A}_1 \right) - \mathbf{A}_1 \right]$,
$\mathbf{R}_{\Gamma_1^-\Gamma_2^+} = \mathbf{A}_2^{-1} \left[\mathbf{A}_4 \left(\mathbf{A}_8 - \mathbf{A}_5\mathbf{A}_2^{-1}\mathbf{A}_4 \right)^{-1} \left(\mathbf{A}_7 - \mathbf{A}_5\mathbf{A}_2^{-1} \right) - \mathbf{A}_3 \right]$, $\mathbf{R}_{\Gamma_2^-\Gamma_1^+} = - \left(\mathbf{A}_8 - \mathbf{A}_5\mathbf{A}_2^{-1}\mathbf{A}_4 \right)^{-1}$
$\left[\mathbf{A}_5 - \mathbf{A}_5\mathbf{A}_2^{-1}\mathbf{A}_1 \right]$ and $\mathbf{R}_{\Gamma_2^-\Gamma_2^+} = - \left(\mathbf{A}_8 - \mathbf{A}_5\mathbf{A}_2^{-1}\mathbf{A}_4 \right)^{-1} \left[\mathbf{A}_7 - \mathbf{A}_5\mathbf{A}_2^{-1} \right]$. By substitutions of Eqq. (17) in the first two equations of (16), it results:

$$\mathbf{w}_E^{\Gamma_1^+} = \mathbf{H}_1^{-1} \left(\boldsymbol{\Delta}_1 + \mathbf{H}_2\boldsymbol{\Delta}_2 \right)$$
$$\mathbf{w}_E^{\Gamma_2^+} = \mathbf{H}_3^{-1} \left(\mathbf{H}_4\boldsymbol{\Delta}_1 + \mathbf{H}_5\boldsymbol{\Delta}_2 \right)$$

(18)

with $\mathbf{H}_1 = \left(\mathbf{I} - \mathbf{R}_{\Gamma_1^- \Gamma_1^+}\right) - \mathbf{R}_{\Gamma_1^- \Gamma_2^+}\left(\mathbf{I} - \mathbf{R}_{\Gamma_2^- \Gamma_2^+}\right)^{-1}\mathbf{R}_{\Gamma_2^- \Gamma_2^+}; \quad \mathbf{H}_2 = \mathbf{R}_{\Gamma_1^- \Gamma_2^+}\left(\mathbf{I} - \mathbf{R}_{\Gamma_2^- \Gamma_2^+}\right);$

$\mathbf{H}_3 = \mathbf{I} - \mathbf{R}_{\Gamma_2^- \Gamma_2^+}; \quad \mathbf{H}_4 = \mathbf{R}_{\Gamma_2^- \Gamma_1^+}\mathbf{H}_1 - 1; \quad \mathbf{H}_5 = \mathbf{I} - \mathbf{R}_{\Gamma_2^- \Gamma_1^+}\mathbf{H}_1^{-1}\mathbf{R}_{\Gamma_1^+ \Gamma_2^-}\left(\mathbf{I} - \mathbf{R}_{\Gamma_2^- \Gamma_2^+}\right).$

At this point, the classical homogenized elasticity matrix can be evaluated adopting the Hill-Mandel macro-homogeneity condition, i.e. the equality between the strain energy at the both the macroscopic scale $\mathcal{E}_M$ and the microscopic scale $\mathcal{E}_m(\Delta_1, \Delta_2)$:

$$\mathcal{E}_M = \mathcal{E}_m(\Delta_1, \Delta_2) \tag{19}$$

with

$$\mathcal{E}_M = \frac{1}{2}A\mathbf{E}^T\mathbf{C}\mathbf{E} \qquad \text{and} \qquad \mathcal{E}_m(\Delta_1, \Delta_2) = \frac{1}{2}\mathbf{b}_E^T\mathbf{w}_E \tag{20}$$

where A is the area of the Periodic Cell. The unknown terms in Eq. (19) are the components of $\mathbf{C}$ (reported in Eq. (20)). They can be evaluated according to the following steps: i) find $\mathbf{w}_E$ via Eqq. (18) and (17); ii) obtain $\mathbf{b}_E$ adopting Eq. (12); iii) in $\mathcal{E}_m$, Eq. (20), explicit the dependence of Δ_1 and Δ_2 on the macro-strain components via Eq. (14). In this way a quadratic form in terms of the macro-strain components is obtained; iv) evaluate the components of $\mathbf{C}$ adopting Eq. (19).

The considered beam model is very simplified and it is noteworthy that more reliable results can be obtained if the length of the beam is modeled more accurately. A possible way forward would be to consider slightly longer beam lengths (including in the length also the thickness t of the ring), following the examples of (Chen et al., 2013) which proposed a beam lattice model where the axial stiffness was neglected.

It is noteworthy that for the anti-tetrachiral geometry, the micropolar homogenization model proposed by (Scarpa et al., 2007; Bacigalupo and Gambarotta, 2014a) seems difficult to apply due to the lack of a central ring on which all the ligaments converge. Therefore, the alternative model, already presented, has been conceived to estimate the overall constitutive first order constants.

3.2. Continuous model: Cauchy-type model

The standard first order computational homogenization, as in Guedes and Kikuchi (1990); Ghosh et al. (1996); Miehe (2002), is here adopted, through the FE elastic analysis, to evaluate the effective elastic properties of cellular solids characterized by anti-tetrachiral lattice microstructure. The Cauchy model is used at both scales. Accordingly, at the typical macroscopic material point $\mathbf{X} = \{X_1, X_2\}^T$ the displacement vector $\mathbf{U} = \{U_1, U_2\}^T$ is defined and the strain vector is derived by

applying the kinematic operator, resulting as:

$$\boldsymbol{E} = \left\{ \begin{array}{c} E_{11} \\ E_{22} \\ \sqrt{2}E_{12} \end{array} \right\} = \mathbf{D} \left\{ \begin{array}{c} U_1 \\ U_2 \end{array} \right\} \qquad \text{with } \mathbf{D}(\mathbf{X}) = \left[\begin{array}{cc} \bullet_{,1} & 0 \\ 0 & \bullet_{,2} \\ \sqrt{2}\bullet_{,2} & \sqrt{2}\bullet_{,1} \end{array} \right] \tag{21}$$

The constitutive equations at the macro-level, in the tensorial representation, take the form :

$$\left\{ \begin{array}{c} \Sigma_{11} \\ \Sigma_{22} \\ \sqrt{2}\Sigma_{12} \end{array} \right\} = \mathbf{C} \left\{ \begin{array}{c} E_{11} \\ E_{22} \\ \sqrt{2}E_{12} \end{array} \right\} \qquad \text{with } \mathbf{C}(\mathbf{X}) = \left[\begin{array}{ccc} C_{1111} & C_{1122} & 0 \\ C_{1122} & C_{2222} & 0 \\ 0 & 0 & 2C_{1212} \end{array} \right] \tag{22}$$

where Σ_{12} is the shear stress and $\mathbf{C}$ is the overall elasticity tensor.

At the micro-level, the corresponding strain $\boldsymbol{\varepsilon}$ and stress $\boldsymbol{\sigma}$ measures together with the elasticity matrix $\mathbf{c}$ are defined in a similar way as in Eqq.(21) and (22).

The classical first order multi-scale scheme is defined in the framework of a strain driven approach. The vector $\mathbf{E}$ is, thus, used as input quantity for the periodic cell and a properly defined Boundary Value Problem (BVP) is solved with periodic boundary conditions (PBCs). The displacement field solution of the BVP at the typical point $\mathbf{x} = \{x_1, x_2\}^T$ of the periodic cell can be defined as the superposition of two fields, resulting in the same expression already presented in Eq. (1) and is here reported in compact form for the sake of clarity:

$$\mathbf{u}(\mathbf{X}, \mathbf{x}) = \mathbf{u}^*(\mathbf{X}, \mathbf{x}) + \tilde{\mathbf{u}}(\mathbf{X}, \mathbf{x}) \tag{23}$$

where $\mathbf{u}^*(\mathbf{X}, \mathbf{x}) = \mathbf{E}(\mathbf{X})\mathbf{x}$ is an assigned field depending on the macro-strain tensor and $\tilde{\mathbf{u}}(\mathbf{X}, \mathbf{x})$ is a periodic perturbation field arising from the presence of heterogeneities.

The PBCs are imposed between corresponding points $\mathbf{x}^+$ and $\mathbf{x}^-$ belonging to opposite edges of the periodic cells, see Figure 5, leading to the following constraint relations:

- Vertices of the periodic cell:

  $u_i(\mathbf{X}, \mathbf{x}) = \mathbf{E}(\mathbf{X})\mathbf{x}_i \qquad i = 1, .., 4$

- Points on the edges:

  $u^+(\mathbf{X}, \mathbf{x}) - u^-(\mathbf{X}, \mathbf{x}) = \mathbf{E}(\mathbf{X})\Delta\mathbf{x} \qquad \text{with} \qquad \Delta\mathbf{x} = \mathbf{x}^+ - \mathbf{x}^-$

The macroscopic stress $\boldsymbol{\Sigma}(\mathbf{X})$ and strain $\mathbf{E}(\mathbf{X})$ measures are linked to the respective microscopic ones, $\boldsymbol{\sigma}(\mathbf{x})$ and $\varepsilon(\mathbf{x})$, through the following spatial averages:

$$\boldsymbol{\Sigma}(\mathbf{X}) = \langle \boldsymbol{\sigma}(\mathbf{X}, \mathbf{x}) \rangle_\omega, \qquad \mathbf{E}(\mathbf{X}) = \langle \varepsilon(\mathbf{X}, \mathbf{x}) \rangle_\omega \tag{24}$$
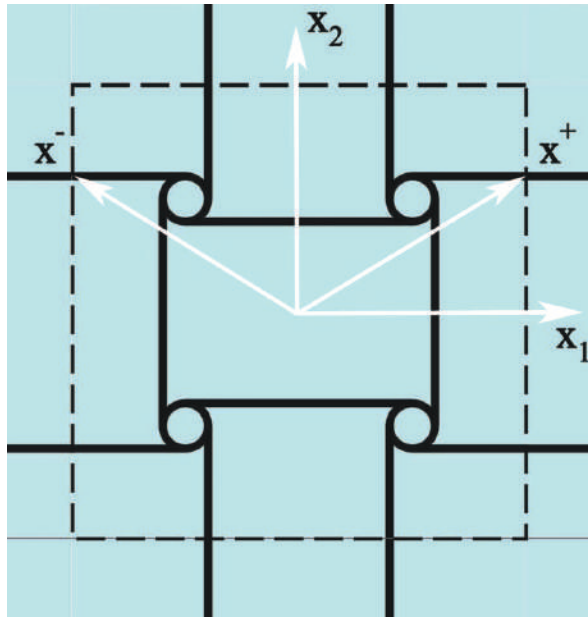
Figure 5: Periodic Boundary conditions: corresponding points $\mathbf{x}^+$ and $\mathbf{x}^-$ on the edges of the periodic cell. The origin of the reference frame is placed in the geometric center of the Periodic Cell.

where the brackets $\langle \cdot \rangle_\omega = \frac{1}{2} \int_\omega (\cdot) \, d\omega$ denote the average over the area ω of the periodic cell.

It is possible to express the mean value of the microscopic strain energy of the periodic cell $\mathcal{E}_m = \frac{\omega}{2} \left\langle \varepsilon \left(\mathbf{X}, \mathbf{x} \right)^T \mathbf{c} \left(\mathbf{x} \right) \varepsilon \left(\mathbf{X}, \mathbf{x} \right) \right\rangle_\omega$ in terms of the macroscopic strain $\mathbf{E} \left(\mathbf{X} \right)$ as:

$$\varepsilon \left(\mathbf{X}, \mathbf{x} \right) = \mathbf{B} \left(\mathbf{x} \right) \mathbf{E} \left(\mathbf{X} \right) \tag{25}$$

where $\mathbf{B} \left(\mathbf{x} \right)$ is a localization matrix depending on the periodic field solution of the BVP at the periodic cell level with PBCs.

Likewise, at the macroscopic level the strain energy $\mathcal{E}_M$ at a typical point $\mathbf{X}$ of the homogenized continuum can be clearly stated as a function of the macroscopic strain vector resulting in:

$$\mathcal{E}_M = \frac{1}{2} \mathbf{E} \left(\mathbf{X} \right)^T \mathbf{C} \left(\mathbf{X} \right) \mathbf{E} \left(\mathbf{X} \right) A \tag{26}$$

where A is the area of the Periodic Cell. By exploiting the the Hill-Mandel macro-homogeneity condition, establishing that $\mathcal{E}_M = \mathcal{E}_m$, the classical homogenized elasticity matrix can be evaluated as:

$$\mathbf{C} \left(\mathbf{X} \right) = \langle \mathbf{B} \left(\mathbf{x} \right)^T \mathbf{c} \left(\mathbf{x} \right) \mathbf{B} \left(\mathbf{x} \right) \rangle_\omega \tag{27}$$

It is noteworthy that in Eqq. (24) and (27) the perturbation terms of the displacements do not influence the homogenized values since are characterized by zero averages in the Periodic Cell domain. Let $(\mathbf{a}_1, \mathbf{a}_2)$ be the standard basis $(\mathbf{e}_1, \mathbf{e}_2)$ rotated by the counterclockwise angle ϑ about an axis through the origin. An interesting and comprehensive description of the elastic homogenized response

13

can be obtained by evaluating $E_{hom}(\vartheta)$ and $\nu_{hom}(\vartheta)$ obtained for tension along the direction identified by the unit vector $\mathbf{a}_1$ inclined at an angle ϑ with respect to the reference unit vector $\mathbf{e}_1$. The elastic compliance tensor can be defined as $\mathbf{D} = \mathbf{C}^{-1}$ and the compliance in the new rotated frame system $\mathbf{D}^\vartheta$ is a fourth order tensor whose generic component obeys the following transformation law:

$$D_{ijkl}^\vartheta = Q_{im}Q_{jn}Q_{ko}Q_{lp}D_{mnop}. \tag{28}$$

where the rotation tensor $\mathbf{Q}(\vartheta)$, describing the rotation of $\mathbf{a}_1$ with respect to $\mathbf{e}_1$, has the same representation as in Eq. (6).

The resulting elastic moduli as a function of ϑ is equal to:

$$E_{hom}(\vartheta) = \frac{1}{D_{1111}^\vartheta} \tag{29}$$

where, exploiting the material symmetries of the anti-tetrachiral cellular solid, it results:

$$D_{1111}^\vartheta = D_{1111}cos\vartheta^4 + 2(D_{1122} + 2D_{1212})cos\vartheta^2 sin\vartheta^2 + D_{2222}sin\vartheta^4 \tag{30}$$

while the Poisson's ratio can be evaluated as:

$$\nu_{hom}(\vartheta) = -\frac{D_{1122}^\vartheta}{D_{1111}^\vartheta} \tag{31}$$

with

$$D_{1122}^\vartheta = (D_{1111} + D_{2222} - 4D_{1212})cos\vartheta^2 sin\vartheta^2 + D_{1122}(cos\vartheta^4 + sin\vartheta^4) \tag{32}$$

3.3. Numerical investigation

The effective elastic constants of the anti-tetrachiral lattice are evaluated via numerical tests carried out considering different mechanical and geometrical parameters.

First, the results obtained adopting the discrete beam lattice model and the continuous model are compared. The geometric configuration of the lattice is shown in Figure 3 where a periodic cell is reported. The radius of the ring is $R = 5 \ mm$, the distance between the centers of two neighboring rings is $L = 25 \ mm$ and the constant thickness of the ligaments is $t = 1.5 \ mm$. In order to adequately exploit the capabilities of both models, it is assumed that: i) rigid nodes are considered in the discrete model while in the continuous model the rings are filled with a material characterized by the same elastic properties of the ligaments, $E_r/E_i = 1$; ii) no matrix between the ligaments is considered, $E_m/E_i = 0$. The elastic parameters are Young's Modulus $E_i = 1.6 \ GPa$ and Poisson ratio $\nu_i = 0.36$ of the ligaments. For the solid model, plane stress conditions are considered with an out-of-plane

14

thickness equal to 1 mm.

In Figure 6(a) the elastic modulus E_{hom}, normalized by $E_{hom}^{ort} = \Sigma_{11}/E_{11}(= \Sigma_{22}/E_{22})$, versus the inclination angle ϑ is shown for the beam lattice model (green line) and for the solid model (red line). Similarly, ν_{hom} is reported in blue line (beam lattice model) and in black line (solid model). A strongly anisotropic behavior is observed with pronounced variations in the elastic properties as the ϑ slightly varies. Moreover, it is remarkable that the material exhibit auxeticity only for given ranges of ϑ. The results are in satisfactory agreement. This confirms the reliability of the beam lattice model, at least for the cases where the matrix can be neglected.

A further comparison is carried out as the ratio L/R varies. In Table 1 the values of the effective constants C_{1111}, C_{2222}, C_{1122} and C_{1212} together with those of the correspondent Young's modulus E_{hom}^{ort} and Poisson ratio $\nu_{hom}^{ort} = -E_{22}/E_{11}(= -E_{11}/E_{22})$, associated with a state of uniaxial tensile stress along the orthotropic axes (i.e. evaluated adopting Eqq. (32) and (31) with $\vartheta = 0$, respectively) are reported for L/R ranging between 3 and 10. The beam lattice model is considered in this case. In Table 2 the same results of Table 1 are collected in the case of the continuous model. It is noteworthy that the beam lattice model tends to underestimate E_{hom}^{ort}, and, at the same time, to slightly overestimate ν_{hom}^{ort}. The Poisson's ratio are almost constant with variations in the third decimal place. In Figures 6(b), (c) and (d), E_{hom}/E_{hom}^{ort}, E_{hom}/E_i and ν_{hom} versus ϑ are reported, respectively. The green lines refer to $L/R = 3$, the red lines to $L/R = 5$ and the blue line to $L/R = 10$, both for the beam lattice model (dashed lines) and the solid model (solid lines). In Figure 6(d) it emerges that, as L/R decreases, the curves are lowered and for $L/R = 10$ the Poisson's ratio is negative for each ϑ. For the same case, in which the matrix between the ligaments is neglected, a

L/R		C_{1111}	C_{2222}	C_{1122}	C_{1212}		E_{hom}^{ort}	ν_{hom}^{ort}
3		120.89	120.89	-119.11	2.40		3.55	-0.99
4		90.67	90.67	-89.33	1.01		2.66	-0.99
5		72.54	72.54	-71.46	0.52		2.13	-0.99
6		60.45	60.45	-59.55	0.30		1.77	-0.99
8		45.34	45.34	-44.67	0.13		1.33	-0.99
10		36.27	36.27	-35.73	0.06		1.06	-0.99

Table 1: Beam lattice model. Effective elastic constants $[MPa]$ for different values of L/R.

direct comparison with the experimental results presented in (Alderson et al., 2010) is performed. In Table 3 the values of E_{hom}^{ort} and ν_{hom}^{ort} obtained adopting both the models presented in Sections (3.1) and
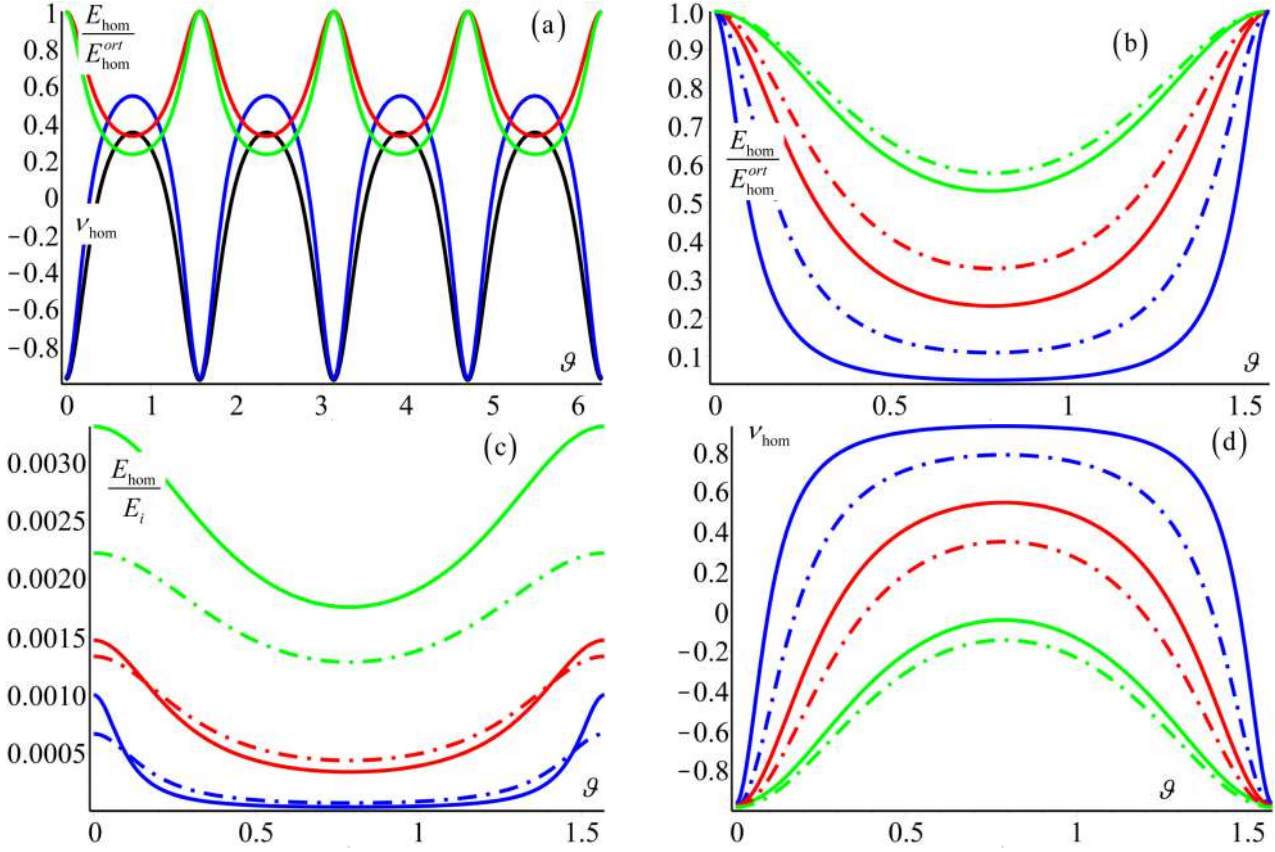
Figure 6: Comparison between beam lattice model and solid model. a) E_{hom}/E_{hom}^{ort} versus ϑ for beam lattice model (green) and solid model (red). ν_{hom} versus ϑ for beam lattice model (blue) and solid model (black); (b)E_{hom}/E_{hom}^{ort} versus ϑ; (c)E_{hom}/E_i versus ϑ ; (d)ν_{hom} versus ϑ. In (b), (c) and (d) dashed lines are referred to beam lattice model and solid lines to solid model and green lines represent $L/R = 3$, red lines $L/R = 5$ and blue lines $L/R = 10$.

L/R		C_{1111}	C_{2222}	C_{1122}	C_{1212}		E_{hom}^{ort}	ν_{hom}^{ort}
3		88.48	88.48	-85.80	2.94		5.28	-0.97
4		64.64	64.64	-62.82	0.83		3.59	-0.97
5		50.88	50.88	-49.51	0.35		2.69	-0.97
6		42.24	42.24	-40.99	0.18		2.46	-0.97
8		31.38	31.38	-30.40	0.06		1.93	-0.97
10		24.96	24.96	-24.15	0.03		1.60	-0.97

Table 2: Solid model: $E_m/E_i = 0$. Effective elastic constants $[MPa]$ for different values of L/R.

16

(3.2) are compared against the experimental data. The geometric ratio considered is $L/R = 5$. The numerical results are satisfactory. The beam lattice model, despite its strong simplifying assumptions, predicts the auxeticity of the material and estimates very well the Poisson's ratio, while the Young's modulus is underestimated of about 30%. Slightly more accurate results could be achieved if the length of the beams were redefined as in (Scarpa et al., 2007), where also the the thickness t (see Figure 3) is included in the length of the rigid ends. Adopting the continuous model, instead, both moduli are in good agreement with experimental results and the percentage difference in terms of Young's moduli drops to about 10 %. The observed differences are likely due to the difficulty of obtaining reliable experimental results in such an anisotropic material, since slightest variations in the specimen inclination in the testing machine strongly affect the results.

Case	E_{hom}^{ort}	ν_{hom}^{ort}
Experimental (Alderson et al., 2010)	3.11	-0.98
Beam Lattice	2.13	-0.99
Solid	2.69	-0.97

Table 3: $E_m/E_i = 0$ and $L/R = 5$. Comparison between experimental (Experimental) results obtained by (Alderson et al., 2010), beam lattice model (Beam Lattice) and Solid model (Solid) results.
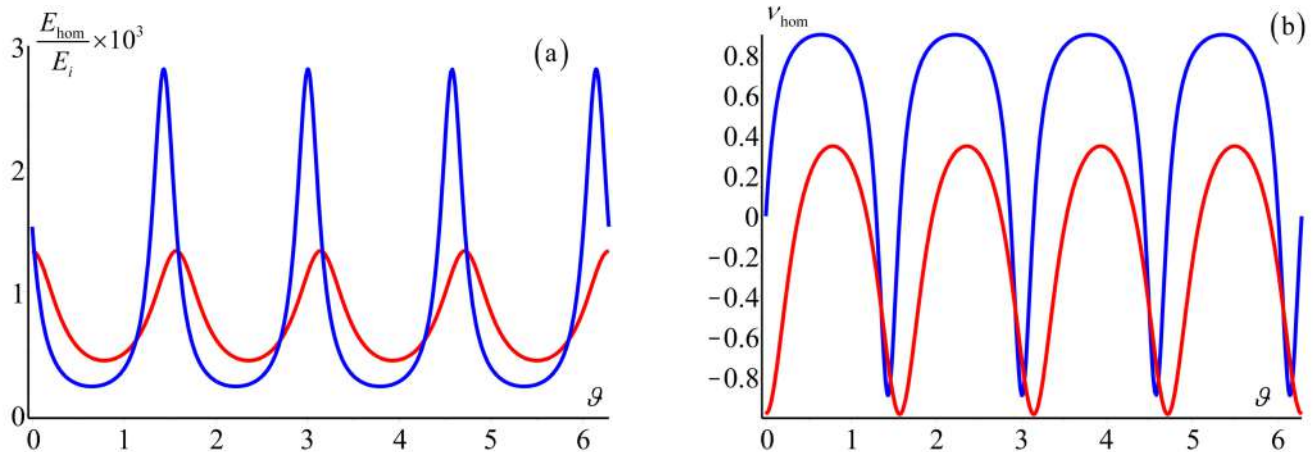
Figure 7: $E_m/E_i = 0$ and $L/R = 5$. Comparison between anti-tetrachiral (red lines) and tetrachiral (blue lines) cellular solids. a) E_{hom}/E_i versus ϑ; (b) ν_{hom} versus ϑ. The results have been obtained adopting different beam lattice models: the model presented in Section 3.1 in the case of the anti-tetrachiral geometry and the model proposed in (Bacigalupo and Gambarotta, 2014a) in the case of the tetrachiral geometry.

In order to highlight the specificity of the studied class of micro-structures, it can be interesting to compare the responses of anti-tetrachiral and tetrachiral cellular solids in terms of homogenized

elastic moduli. Considering the same material properties and geometric parameters already chosen in the case presented in Table 3, two different beam lattice models are adopted: the model presented in Section 3.1 in the case of the anti-tetrachiral geometry and the model proposed in (Bacigalupo and Gambarotta, 2014a) for the tetrachiral geometry. To be noted is that, since in the models the length of the ligaments is assumed to be equal, due to the different geometrical arrangement, the distance between the centers of the rings is slightly lower in the tetrachiral cellular solid. In Figures 7(a) and (b) E_{hom}/E_i and ν_{hom} versus ϑ are plotted, respectively. The red lines correspond to the anti-tetrachiral geometry, while the blue lines correspond to the tetrachiral geometry. It stands to reason that both geometries display an anisotropic behavior (more evident in the tetrachiral cellular solid) and are characterized by different material symmetries. The maximum values of E_{hom} are greater (for a broad range of ϑ) in the case of the centrosymmetric tetrachiral geometry, however it appears that the orthotropic anti-tetrachiral geometry shows a more pronounced auxeticity. Although this example is not meant to be exhaustive, it qualitatively outlines some inherent features of the studied material, that could be crucial in the design of architectured materials with required performances.

At this point, the influence of the elastic matrix between the ligaments on the effective elastic constants of the anti-tetrachiral cellular solids is investigated. For this reason, in the following only the results obtained adopting the computational homogenization technique are shown.

The initial geometric configuration of the lattice is shown in Figure 3. Also in this case, $R = 5\ mm$ and $L = 25\ mm$ and a constant thickness of all portions of inclusions (rings and ligaments) $t = 1.5\ mm$ are considered. The elastic parameters are Young's Modulus $E_i = 1.6\ GPa$ and Poisson ratio $\nu_i = 0.36$ for the ligaments and $E_m/E_i = 10^{-3}$ and $\nu_m = \nu_i$ for the matrix (filling the space between ligaments). In what follows E_r is referred to the Young's modulus of the material possibly filling the rings.

First of all the effect of variations of geometric parameters has been investigated. For this purpose, the ratio between the distance L and the radius R varies, while all the other parameters are left unchanged. It is assumed that $E_r/E_m = 1$.

In Table 4, C_{1111}, C_{2222}, C_{1122} and C_{1212} together with E_{hom}^{ort} and ν_{hom}^{ort}, are reported for L/R between 3 and 10. It is noteworthy that in all the considered cases the material exhibits auxetic features with negative Poisson's ratio whose absolute value reaches its maximum for $L/R = 5$ and decreases as L/R increases. It stands to reason that the matrix has a strong effect in reducing the auxeticity of the material.

In Figure 8(a) a Cartesian diagram showing the trend of E_{hom} normalized with respect to the maximum value E_{hom}^{ort} is plotted versus ϑ. Due to the symmetry only the values for $0 \leq \vartheta \leq \pi/2$ are

18

L/R		C_{1111}	C_{2222}	C_{1122}	C_{1212}		E_{hom}^{ort}	ν_{hom}^{ort}
3		37.68	37.68	-26.44	2.63		19.11	-0.70
4		32.91	32.91	-24.26	1.46		15.02	-0.74
5		29.97	29.97	-22.04	0.29		13.76	-0.74
6		27.54	27.54	-19.87	0.90		13.20	-0.72
8		22.62	22.62	-15.37	0.74		12.18	-0.68
10		20.05	20.05	-12.92	0.69		11.72	-0.64

Table 4: Solid model: $E_m/E_i = 10^{-3}$. Effective elastic constants $[MPa]$ for different values of L/R. It is assumed that $E_r/E_m = 1$.
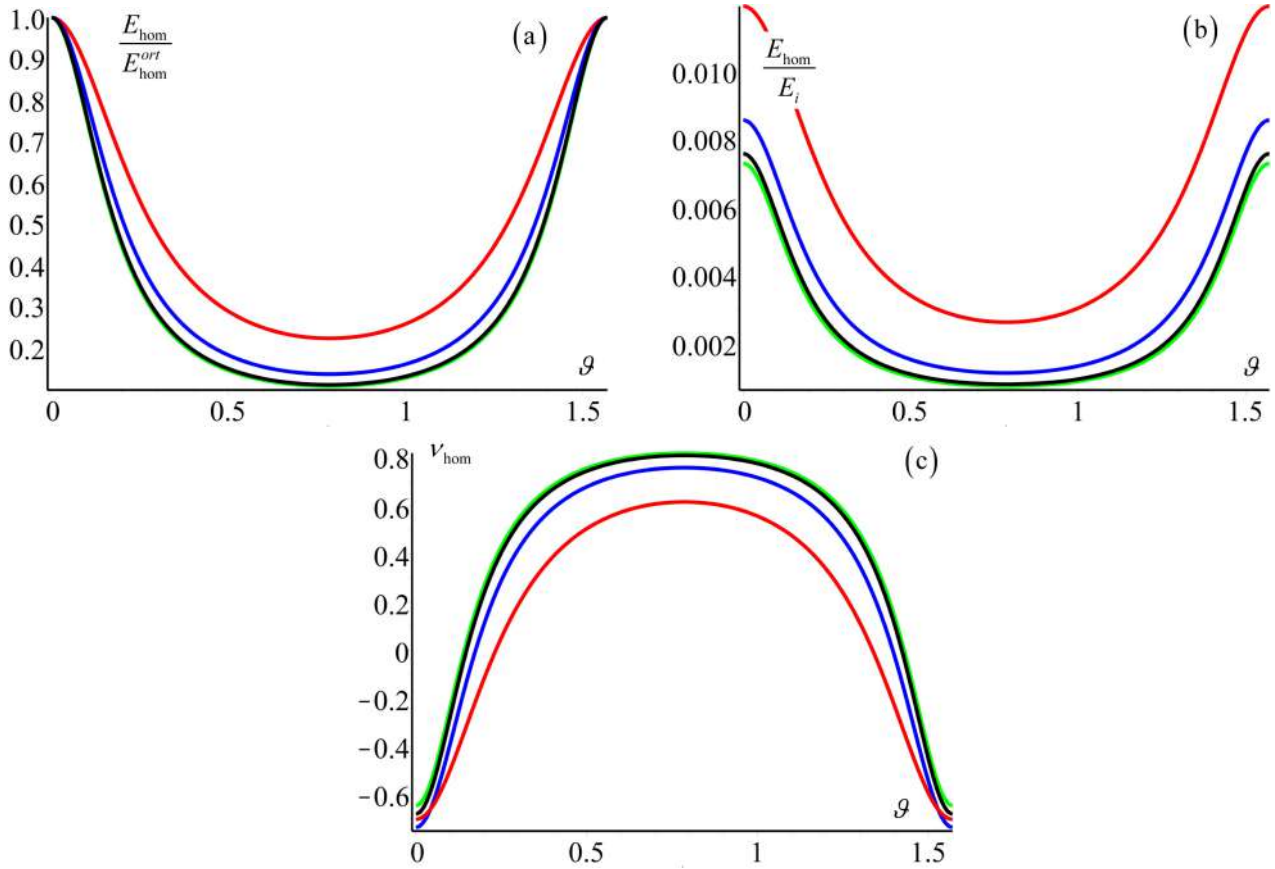
Figure 8: Solid model. (a) E_{hom}/E_{hom}^{ort} versus ϑ; (b)E_{hom}/E_i versus ϑ; (c)ν_{hom} versus ϑ. Red line ($L/R = 3$); blue line ($L/R = 5$); black line ($L/R = 8$); green line ($L/R = 10$). It is assumed that $E_r/E_m = 1$.

shown. The red line corresponds to $L/R = 3$, the blue line to $L/R = 5$, the black line to $L/R = 8$ and, finally, the green line to $L/R = 10$. Qualitatively the trends are similar and, as the ratio L/R increases, the curves are characterized by lower values of the minimum corresponding to $\vartheta = \pi/4$. From a certain point on ($L/R = 8$) the curves overlap each other, giving rise to a response independent on the geometric parameter.

Figure 8(b) shows E_{hom} normalized with respect to the Young's modulus of the ligaments E_i plotted versus ϑ, while, Figure 8(c), shows the variation of the Poisson's ratio ν_{hom} with ϑ. The colors of the curves have the same meanings as in Figure 8(a). Figure 8(c) reveals that there are values of ϑ for which there is a transition from auxetic to non auxetic behavior of the material. Lower values of L/R are characterized by broader ranges of auxetic behaviors.

Moreover, the effect of the elastic properties of the matrix are examined. Considering the geometry in Figure 3, the effective parameters are evaluated for different values of E_m/E_i (with $E_r/E_m = 1$) and the results are collected in Table 5. It emerges that the first case analyzed, i.e. $E_m/E_i = 0$,

E_m/E_i		C_{1111}	C_{2222}	C_{1122}	C_{1212}		E_{hom}^{ort}	ν_{hom}^{ort}
0		23.97	23.97	-22.59	0.28		2.67	-0.94
$1 \cdot 10^{-3}$		29.97	29.97	-22.04	0.29		13.76	-0.74
$1 \cdot 10^{-2}$		65.41	65.41	-12.05	7.90		63.19	-0.18
$1 \cdot 10^{-1}$		287.65	287.65	75.02	71.26		268.08	0.26
$2 \cdot 10^{-1}$		486.93	486.93	153.92	137.75		438.27	0.32
$5 \cdot 10^{-1}$		1026.13	1026.13	361.59	321.35		898.71	0.35

Table 5: Solid model. Effective elastic constants $[MPa]$ for different values of E_m/E_i. It is assumed that $E_r = E_m$.

is characterized by the most pronounced auxeticity with a value of $\nu_{hom}^{ort} = -0.94$. In the other cases, in which a matrix between the ligaments is accounted for, a clear decrease of such property is detected as E_m/E_i increases, up to the case $E_m/E_i = 1 \cdot 10^{-1}$ where the material loses its auxeticity properties. These results suggest that, for a fixed geometry of the cellular solid, different properties can be tuned by varying the properties of the matrix filling the inclusions (i.e. ligaments and rings). In Figure 9(a) the case with $E_m/E_i = 1 \cdot 10^{-3}$ is considered: the red line is E_{hom}/E_{hom}^{ort} and the black line is ν_{hom} versus ϑ ($0 \leq \vartheta \leq 2\pi$). In Figure 9(b) and (c) E_{hom}/E_{hom}^{ort} and ν_{hom} are plotted for different ratios E_m/E_i versus ϑ, respectively. The red line corresponds to $E_m/E_i = 0$, the blue line to $E_m/E_i = 1 \cdot 10^{-2}$, the black line to $E_m/E_i = 1 \cdot 10^{-1}$ and, finally, the green line to $E_m/E_i = 5 \cdot 10^{-1}$.

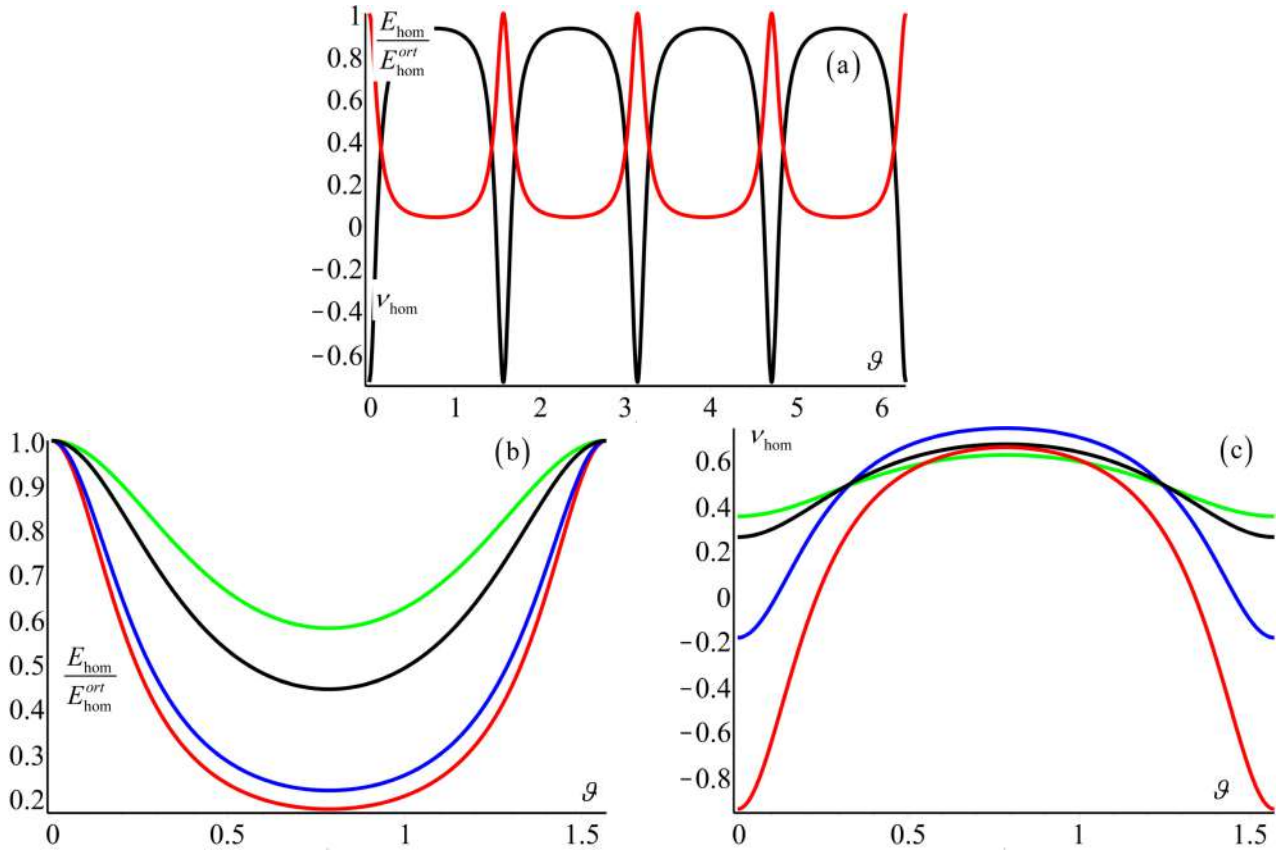A further parametric study concerns the influence of the Young's modulus of the portion of matrix

Figure 9: Solid model.(a) Case $E_m/E_i = 10^{-3}$. Red line: E_{hom}/E_{hom}^{ort} versus ϑ; black line: ν_{hom} versus ϑ; (b)E_{hom}/E_{hom}^{ort} versus ϑ; (c)ν_{hom} versus ϑ. In (b) and (c): red line ($E_r/E_i = 0$); blue line ($E_r/E_i = 1 \cdot 10^{-2}$); black line ($E_r/E_i = 1 \cdot 10^{-1}$); green line ($E_r/E_i = 5 \cdot 10^{-1}$). It is assumed that $E_r = E_m$.

21

possibly included in the ring (E_r) on the global elastic parameters. In Table 6 the values of the effec-

E_r/E_i	C_{1111}	C_{2222}	C_{1122}	C_{1212}	E_{hom}^{ort}	ν_{hom}^{ort}
$1 \cdot 10^{-3}$	29.97	29.97	-22.04	0.29	13.76	-0.74
$1 \cdot 10^{-2}$	32.43	32.43	-24.50	1.09	13.93	-0.76
$1 \cdot 10^{-1}$	44.05	44.05	-36.06	1.16	14.53	-0.82
$2 \cdot 10^{-1}$	48.48	48.48	-40.45	1.18	14.73	-0.83
$5 \cdot 10^{-1}$	52.88	52.88	-44.80	1.20	14.92	-0.84
1	55.01	55.01	-46.90	1.21	15.01	-0.85

Table 6: Effective elastic constants $[MPa]$ for different values of E_r with $E_m/E_i = 10^{-3}$.

tive constants are reported, showing that in all cases the Poisson's ratio is negative and its absolute value grows as E_r grows, for a fixed value of $E_m/E_i = 10^{-3}$. In Figure 10(a) E_{hom} versus $0 \leq \vartheta \leq 2\pi$ is drawn in red line, while ν_{hom} versus ϑ in black line in the case of $E_r/E_i = 1$. In Figure 10(b), instead, E_{hom}/E_{hom}^{ort} versus $0 \leq \vartheta \leq \pi$ is shown for two values of E_r/E_i ($E_r/E_i = 1 \cdot 10^{-3}$ red line; $E_r/E_i = 1$ green line). The two curves are almost overlapping each other. Figure 10(c), showing ν_{hom} versus ϑ for the same two values of E_r/E_i ($E_r/E_i = 1 \cdot 10^{-3}$ red line; $E_r/E_i = 1$ green line), highlights very low differences between the two curves and, in particular, the red curve is slightly moved upwards.

The results show the existence of large variations in linear elastic constants and degree of anisotropy, which can be achieved by changing the lattice geometry parameters.
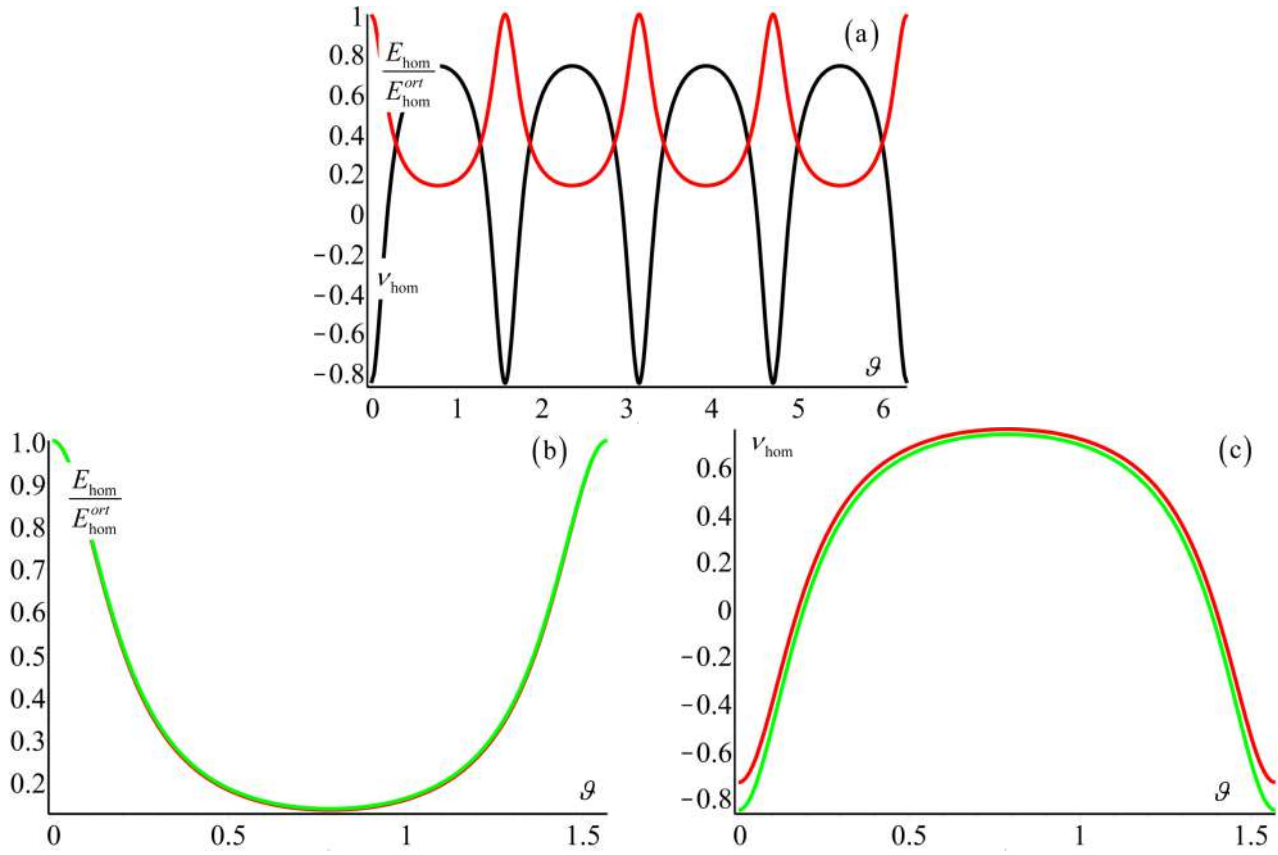
Figure 10: Solid model.(a) Case $E_m/E_i = 10^{-3}$ and $E_r/E_i = 1$. Red line: E_{hom}/E_{hom}^{ort} versus ϑ; black line: ν_{hom} versus ϑ; (b)E_{hom}/E_{hom}^{ort} versus ϑ; (c)ν_{hom} versus ϑ. In (b) and (c): red line ($E_r/E_i = 1 \cdot 10^{-3}$); green line ($E_r/E_i = 1$).

23

4. Dynamic properties of composite materials

The dispersion properties of the periodic anti-tetrachiral cellular solid are investigated adopting the rigorous Floquet-Bloch theory. The exact wave dispersion relations (in terms of frequency versus wave number) for harmonic propagating waves are, indeed, derived through the solution of a well-posed spectral problem for wave dispersion in undamped media.

The details of the BVP defined on the Periodic Cell, with ad-hoc boundary conditions, are reported in the following.

The starting point of the rigorous Floquet-Bloch approach is the set of partial differential equations describing the dynamic balance at the microscopic level, i.e.:

$$div\left(\boldsymbol{\sigma}\left(\mathbf{x},t\right)\right) = \rho\left(\mathbf{x}\right)\ddot{\mathbf{u}}\left(\mathbf{x},t\right) - \mathbf{f}\left(\mathbf{x},t\right) \tag{33}$$

where $\boldsymbol{\sigma}\left(\mathbf{x},t\right)$ is the stress tensor of a material point $\mathbf{x}$ at time t; $\rho\left(\mathbf{x}\right)$ is the the mass density; $\ddot{\mathbf{u}}\left(\mathbf{x},t\right)$ is the acceleration evaluated as second derivative with respect to time of the microscopic displacement vector $\mathbf{u}\left(\mathbf{x},t\right)$ and $\mathbf{f}\left(\mathbf{x},t\right)$ is the body force vector.

The stress tensor can be expressed by the elastic constitutive equation $\boldsymbol{\sigma}\left(\mathbf{x},t\right) = \mathbf{c}\left(\mathbf{x}\right)\boldsymbol{\varepsilon}\left(\mathbf{x},t\right)$ and the strain tensor, in turn, by exploiting the compatibility equations $\boldsymbol{\varepsilon}\left(\mathbf{x},t\right) = sym\nabla\mathbf{u}\left(\mathbf{x},t\right)$.

The Floquet-Bloch approach consists in solving the spectral problem, obtained by the Fourier transform in t of Equation (33), and defined as:

$$div\left(\mathbf{c}\left(\mathbf{x}\right)\nabla\widehat{\mathbf{u}}\left(\mathbf{x}\right)\right) + \omega^2\rho\left(\mathbf{x}\right)\widehat{\mathbf{u}}\left(\mathbf{x}\right) = \mathbf{0} \tag{34}$$

where the constitutive fourth order tensor has the property that $\mathbf{c}\left(\mathbf{x}\right)\mathbf{Z} = \mathbf{c}\left(\mathbf{x}\right)sym\mathbf{Z},\forall\ \mathbf{Z}$; ω is the unknown angular frequency and $\widehat{\mathbf{u}}\left(\mathbf{x}\right)$ is the displacement field in the frequency space. The equations of motion and the wave equation are, thus, specialized to the case of centro-symmetric periodic cells and orthotropic material at the macro-scale, conditions that are suitable to the material here analyzed.

The problem expressed in Eq. (34) must satisfy proper boundary conditions (BCs) on the Periodic Cell. Due to the periodicity of the medium, the following quasi-periodic BCs are imposed:

$$\begin{aligned}\widehat{\mathbf{u}}\left(\mathbf{x}^+\right) &= e^{i\left(\mathbf{k}\Delta\mathbf{x}\right)}\widehat{\mathbf{u}}\left(\mathbf{x}^-\right)\\\widehat{\boldsymbol{\sigma}}\left(\mathbf{x}^+\right)\mathbf{n}^+ &= -e^{i\left(\mathbf{k}\Delta\mathbf{x}\right)}\widehat{\boldsymbol{\sigma}}\left(\mathbf{x}^-\right)\mathbf{n}^-\end{aligned} \tag{35}$$

where $\mathbf{k} = k\mathbf{m}$ is the wave vector, with k being the wave number (only the real part is considered, since an undamped medium is taken into account); $\mathbf{m}$ is the unit vector of propagation; $\mathbf{n}$ is the outward normal unit vector ($\mathbf{n}^+$ and $\mathbf{n}^-$ are defined on the right/top and on the left/bottom edges,

respectively) at $\mathbf{x}^+$ and $\mathbf{x}^-$ on the Periodic Cell boundary (see Figure 5), $\Delta\mathbf{x} = \mathbf{x}^+ - \mathbf{x}^-$ and $\widehat{\boldsymbol{\sigma}}(\mathbf{x})$ is the stress tensor in the frequency space ($\widehat{\boldsymbol{\sigma}} = \mathbf{c}\widehat{\boldsymbol{\varepsilon}}$).

The solution of the Floquet-Bloch problem is obtained by using a FE model of the Periodic Cell implemented in the Structural Mechanics Module, COMSOL 4.3 (COMSOL Multiphysics ®, 2012). This approach, thus, involves the solution of a fine-scale problem that can be computationally burdensome.

A valuable alternative, that works fine in the case of low frequency elastic wave propagation (i.e. in the long wavelength limit), is the use of an equivalent homogeneous model to describe the actual heterogeneous medium. Here a classical (Cauchy) homogenized continuum is considered, that provides reliable results when the size of the heterogeneities is negligible in comparison with the structural size.

It has been shown that, considering a higher order homogenized continuum (Nemat-Nasser et al., 2011; Bacigalupo and Gambarotta, 2014b), the dispersion curve provides a good estimation of the acoustic branch of the Floquet-Bloch spectrum, i.e. the lowest branch of the spectrum, for a wide range of wavelengths. When a Cauchy continuum is, instead, considered as the homogenized medium, a linear relation between the angular frequency and the wave number holds, leading to non-dispersive waves characterized by constant phase velocities.

In the first order case, the equations of motion for the homogenized continuum, without body forces and taking into account the compatibility and the linear elastic constitutive equations, result as:

$$div\,(\mathbf{C}\nabla\mathbf{U}) = \rho_M \ddot{\mathbf{U}} \qquad (36)$$

where $\mathbf{C}$ is the elastic homogenized constitutive fourth order tensor, $\rho_M = \langle \rho(\mathbf{x}) \rangle_\omega$ is the density of the medium averaged over the RVE, $\mathbf{U}$ is the macroscopic displacement field in the homogenized medium. After inserting the harmonic wave solution in Eq. (36), the algebraic spectral problem (Brillouin, 1946) representing an eigenvalue problem, is obtained as:

$$\begin{bmatrix} Q_{11}^2 - \rho_M \hat{c}^2 & Q_{12}^2 \\ Q_{21}^2 & Q_{22}^2 - \rho_M \hat{c}^2 \end{bmatrix} \begin{Bmatrix} \widehat{U}_1 \\ \widehat{U}_2 \end{Bmatrix} = \begin{Bmatrix} 0 \\ 0 \end{Bmatrix}, \qquad (37)$$

where $Q_{ip}^2 = C_{ir_1pr_2}m_{r_1}m_{r_2}$ are the components of the acoustical first order tensor ($\mathbf{m}$ being the unit wave normal corresponding to the direction of $\mathbf{k}$), $C_{ir_1pr_2}$ are the components of the classical overall elastic fourth order tensor, Eq. (27), $\widehat{\mathbf{U}}$ is the macroscopic displacement field in the frequency space, and c the eigenvalue having the meaning of wave phase velocity.

For any wave direction vector $\mathbf{m}$, the eigenvalues $\hat{c}_\varsigma^2$ ($\varsigma = 1, 2$) are the square of the wave velocity in

25

the first order homogenized continuum. The corresponding eigenvectors, whose components are $\widehat{U}_p^\varsigma$ and correspond to the Fourier transform of the macroscopic displacements in the first order homogenized continuum, identify the directions of polarization of the wave.

In order to define dimensionless quantities, the velocity of propagation $\hat{c}_\beta^*$ is defined as to $\hat{c}_\beta^* = \frac{1}{2}\left(\hat{c}_\beta^1 + \hat{c}_\beta^2\right)$, with $\hat{c}_\beta^1$ and $\hat{c}_\beta^2$ being the square roots of the eigenvalues $\hat{c}_\varsigma^2$ ($\varsigma = 1, 2$) solution of the eigenvalue problem for $\mathbf{m} = \mathbf{a}_\beta$, defining the generic direction of wave propagation.

In the case $\mathbf{a}_\beta$ coincides with the orthotropic directions of the material, i.e. $\mathbf{e}_1$ or $\mathbf{e}_2$, the wave velocities become $c_\beta^\alpha = \sqrt{C_{\beta\alpha\beta\alpha}/\rho_M}$, being for ($\alpha = \beta$) the velocity of the compressional waves and for ($\alpha \neq \beta$) the velocity of the shear waves along direction $\mathbf{e}_\beta$ in the classical equivalent continuum ($\alpha, \beta = 1, 2$), for more details see (Bacigalupo and Gambarotta, 2014b).

As an example, a specific anti-tetrachiral cellular solid is considered. The geometry is the same described in Figure 2 with $R = 5\ mm$, $t = 1.5\ mm$ and $L = 25\ mm$. The elastic parameters of the ligaments are Young's Modulus $E_i = 1.6\ GPa$ and Poisson ratio $\nu_i = 0.36$, the mass density is $\rho_i = 1565\ kg/m^3$.

The influence of auxetic properties on the Floquet-Bloch spectrum is here analyzed, both with and without the presence of the matrix between the ligaments.

In particular, the relation between microstructural properties, which are evaluated in terms of Young's modulus ratio (E_m/E_i; E_r/E_i) of ligaments and matrix, and the existence, the position and the frequency range of band gaps is investigated.

The values of the dimensionless angular frequency $\omega d_\beta/2\pi\hat{c}_\varsigma^*$, expressed in terms of the dimensionless wave-number $k d_\beta$ (with $\beta = 1, 2$ and $d_1 = d_2 = L$), are shown in the following figures.

First, the case with no matrix filling the gaps between ligaments ($E_m/E_i = 0$) is considered and $E_r = E_m$, i.e. the rings are empty.

The eigenvalues of the system for waves propagating in the $\mathbf{e}_2$ direction are: $\hat{c}_2^1 = 33.63\ m/s$ and $\hat{c}_2^2 = 308.95\ m/s$. In this case the reference velocity of propagation is $\hat{c}_2^* = 171.29\ m/s$. If, instead, the waves propagate in the $\mathbf{e}_1$ direction, it results $\hat{c}_1^1 = 308.95\ m/s$, $\hat{c}_1^2 = 33.63\ m/s$ and $\hat{c}_1^* = 171.29\ m/s$. Finally, in the case of waves propagating in $\mathbf{a}_3$ direction, with $\mathbf{a}_3 = \sqrt{2}/2\mathbf{e}_1 + \sqrt{2}/2\mathbf{e}_2$ the values are $\hat{c}_1^3 = 304.48\ m/s$, $\hat{c}_2^3 = 62.23\ m/s$ and $\hat{c}_3^* = 183.36\ m/s$.

In Figure 11 the dispersion curves in the Brillouin zone are reported for this case adopting the Floquet-Bloch approach.

In Figure 11(a) the shear waves (red lines) and compressional waves (blue lines) are shown sepa-

rately for waves propagating in both the orthotropic directions $\mathbf{e}_1$ and $\mathbf{e}_2$. It is clear that, by virtue of material symmetry, the overall behavior is the same in both $\mathbf{e}_1$ and $\mathbf{e}_2$ directions. In Figure 11(b), instead, the waves in $\mathbf{a}_3$ direction are show.

In Figure 11(a), considering the global behavior, i.e. the composition of shear and compressional waves, no band gaps are recognized. If, instead, the dispersion functions related to the shear and compressional waves in direction $\mathbf{e}_1$ (and $\mathbf{e}_2$) are considered separately, i.e. red and blue curves, in both cases a band gap is evident: the width is about the same but in the case of compressional waves (blue curve) the frequency band gap is shifted upward (it appears for higher values of $\omega d_\beta / 2\pi \hat{c}_\beta^*$). In the case of waves in $\mathbf{a}_3$ direction (Figure 11(b)), instead, the global behavior shows a frequency band gap characterized by a width of about $\Delta \omega = 0.1 \ 2\pi \hat{c}_\beta^*/d_\beta$, with $\hat{c}_\beta^* = \hat{c}_3^*$ and $d_\beta = d_3 = 2\sqrt{2}L$.
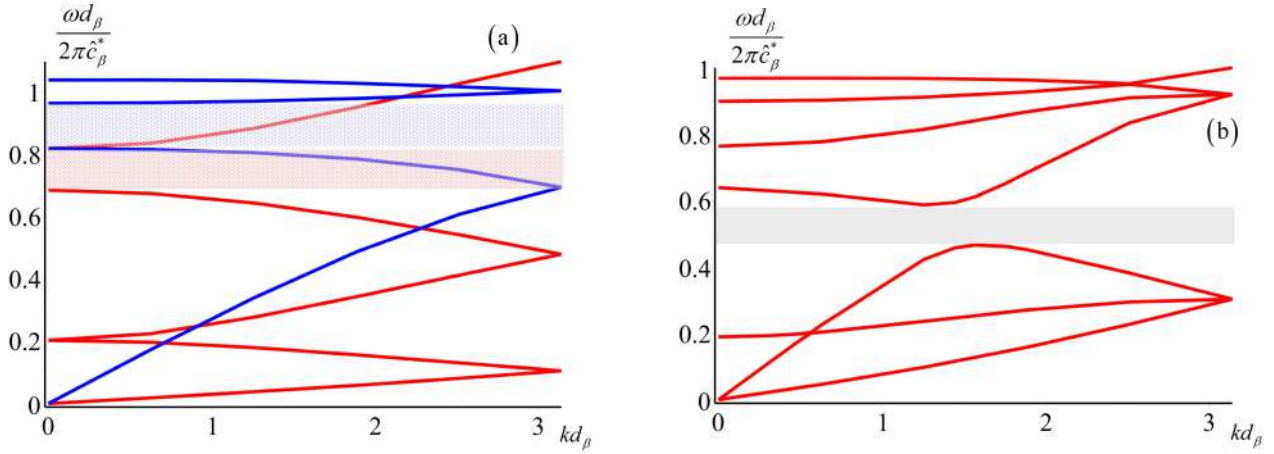
Figure 11: $E_m/E_i = 0$ and $E_r = E_m$. Dispersion curves in the Brillouin zone.(a) waves in $\mathbf{e}_1$ and $\mathbf{e}_2$ directions: shear waves (red) and compressional waves (blue). The partial band gaps are highlighted with dotted rectangles. ; (b)waves in $\mathbf{a}_3$ direction. The full band gap is highlighted with the gray rectangle.

In Figure 12 the dispersion curves associated with shear and compressional waves propagating along the orthotropic axes are represented comparing for each case the results obtained adopting the Floquet-Bloch approach (solid lines), corresponding to a zoom of the Figure 11(a), and the first order homogenization theory (dotted lines). The red curves correspond to shear waves, while the blue curves to compressional waves.

It stands to reason that the first order homogenization theory is able to satisfactorily reproduce the lowest (acoustic) branch of the Bloch spectrum for a wide range of wavelengths. This model, indeed, only describes non-dispersive waves characterized by a linear dependence between the angular frequency ω and the wave-number k (and then between the dimensionless counterparts, i.e $\omega d_\beta / 2\pi \hat{c}_\beta^*$ and kd_β respectively).

27

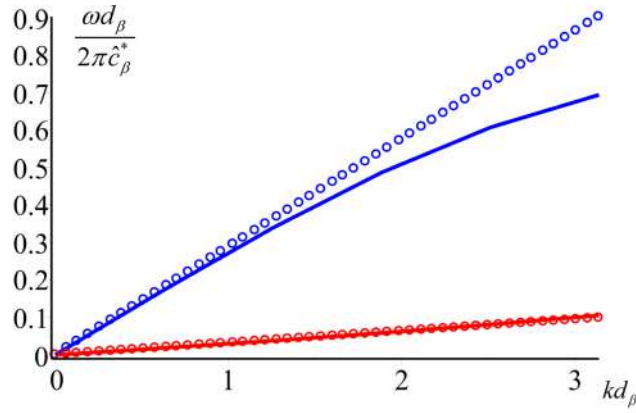At this point, the same case as before is analyzed ($E_m/E_i = 0$) in which the rings are filled with the

Figure 12: $E_m/E_i = 0$ and $E_r = E_m$. Shear (red) and compressional (blue) dispersion curves along the orthotropic axes. Comparison between the Floquet-Bloch approach (solid lines) and the first order computational homogenization theory (dotted lines).

same material as the ligaments, $E_r/E_i = 1$. In this case, the eigenvalues for waves propagating in the $\mathbf{e}_2$ direction are: $\hat{c}_2^1 = 31.74\ m/s$ and $\hat{c}_2^2 = 382.66\ m/s$, with a reference velocity of propagation equal to $\hat{c}_2^* = 207.20\ m/s$. For waves propagating, instead, in the $\mathbf{e}_1$ direction, it results $\hat{c}_1^1 = 382.66\ m/s$, $\hat{c}_1^2 = 31.74\ m/s$ and $\hat{c}_1^* = 207.20\ m/s$. Considering, instead, waves in $\mathbf{a}_3$ direction the values are $\hat{c}_1^3 = 380.08\ m/s$, $\hat{c}_2^3 = 54.58\ m/s$ and $\hat{c}_3^* = 217.33\ m/s$. For this case, in Figures 13 and 14 the same graphs presented in Figures 11 and 12 are shown.

Moreover, the case in which the microstructure is characterized by the presence of both the ligaments
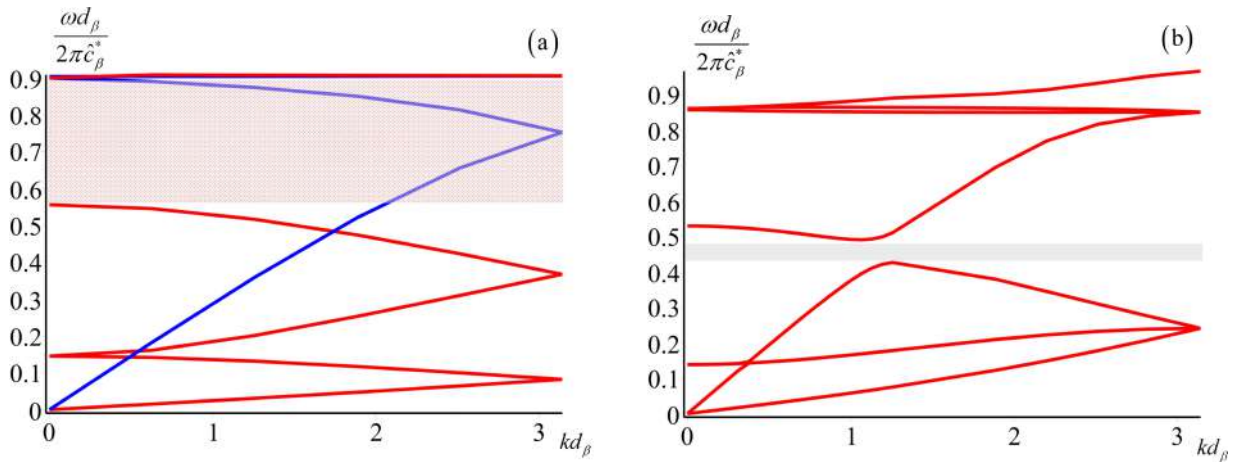
Figure 13: $E_m/E_i = 0$ and $E_r/E_i = 1$. Dispersion curves in the Brillouin zone.(a) waves in $\mathbf{e}_1$ and $\mathbf{e}_2$ directions: shear waves (red) and compressional waves (blue). The partial band gap for shear waves is highlighted with the dotted rectangle; (b)waves in $\mathbf{a}_3$ direction. The full band gap is highlighted with the gray rectangle.

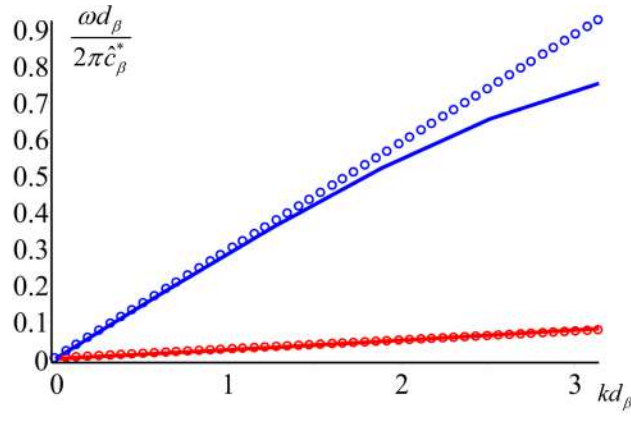and the matrix is considered taking $E_m/E_i = 1 \cdot 10^{-2}$ and $E_r/E_m = 1$. The Poisson's ratio and the

Figure 14: $E_m/E_i = 0$ and $E_r/E_i = 1$. Shear (red) and compressional (blue) dispersion curves along the orthotropic axes. Comparison between the Floquet-Bloch approach (solid lines) and the first order computational homogenization theory (dotted lines).

mass density of the matrix are the same of the ligaments, that is $\nu_m = 0.36$ and $\rho_m = 1565\ kg/m^3$. If the waves propagate in the $\mathbf{e}_2$ direction, the eigenvalues are: $\hat{c}_2^1 = 71.05\ m/s$ and $\widetilde{c}_2^2 = 204.44\ m/s$. In this case the reference velocity of propagation is $\hat{c}_2^* = 137.74\ m/s$. If, instead, the waves propagate in the $\mathbf{e}_1$ direction, it results $\hat{c}_1^1 = 204.44\ m/s$, $\hat{c}_1^2 = 71.05\ m/s$ and $\hat{c}_1^* = 137.74\ m/s$. In the case of waves propagating in $\mathbf{a}_3$ direction the values are $\hat{c}_1^3 = 401.75\ m/s$, $\hat{c}_3^2 = 260.64\ m/s$ and $\hat{c}_3^* = 331.19$ m/s. For this case, in Figures 15 and 16 the same graphs presented in Figures 11 and 12 are shown.

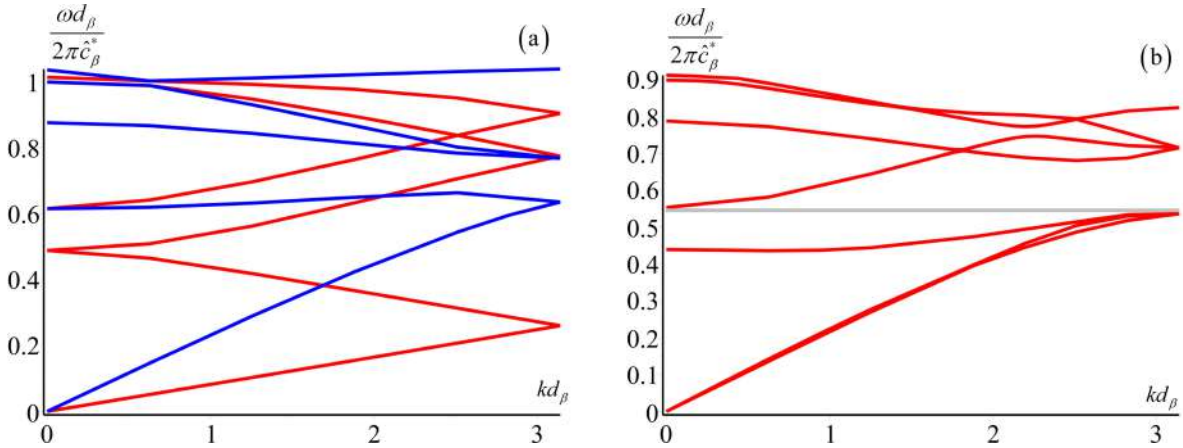Finally, the case with $E_m/E_i = 1 \cdot 10^{-1}$ ($E_r/E_m = 1$) is taken into account. For waves propagating

Figure 15: $E_m/E_i = 1 \cdot 10^{-2}$ and $E_r/E_m = 1$. Dispersion curves in the Brillouin zone.(a) waves in $\mathbf{e}_1$ and $\mathbf{e}_2$ directions: shear waves (red) and compressional waves (blue); (b)waves in $\mathbf{a}_3$ direction. The band gap is highlighted with the gray rectangle.

in the $\mathbf{e}_2$ direction, the eigenvalues are: $\hat{c}_2^1 = 213.39\ m/s$ and $\hat{c}_2^2 = 428.72\ m/s$. In this case the reference velocity of propagation is $\hat{c}_2^* = 321.05\ m/s$. For waves propagating in the $\mathbf{e}_1$ direction, instead, the corresponding values are $\hat{c}_1^1 = 428.72\ m/s$, $\hat{c}_1^2 = 213.39\ m/s$ and $\hat{c}_1^* = 321.05\ m/s$.
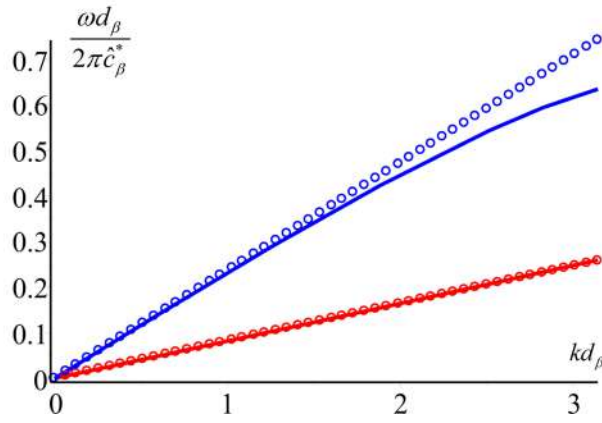
29

Figure 16: $E_m/E_i = 1 \cdot 10^{-2}$ and $E_r/E_m = 1$. Shear (red) and compressional (blue) dispersion curves along the orthotropic axes. Comparison between the Floquet-Bloch approach (solid lines) and the first order computational homogenization theory (dotted lines).

Lastly, in the case of waves propagating in $\mathbf{a}_3$ direction the values are $\hat{c}_1^3 = 401.75\ m/s$, $\hat{c}_2^3 = 260.64$ m/s and $\hat{c}_3^* = 331.19\ m/s$. For this case, in Figures 17 and 18 the same graphs presented in Figures 11 and 12 are shown. Considering Figure 18, it emerges that in this case the acoustic branches are almost linear and the first order homogenization model provides results in a very good agreement with the expected ones.

It is interesting to compare the results obtained in the dimensionless space for the three cases
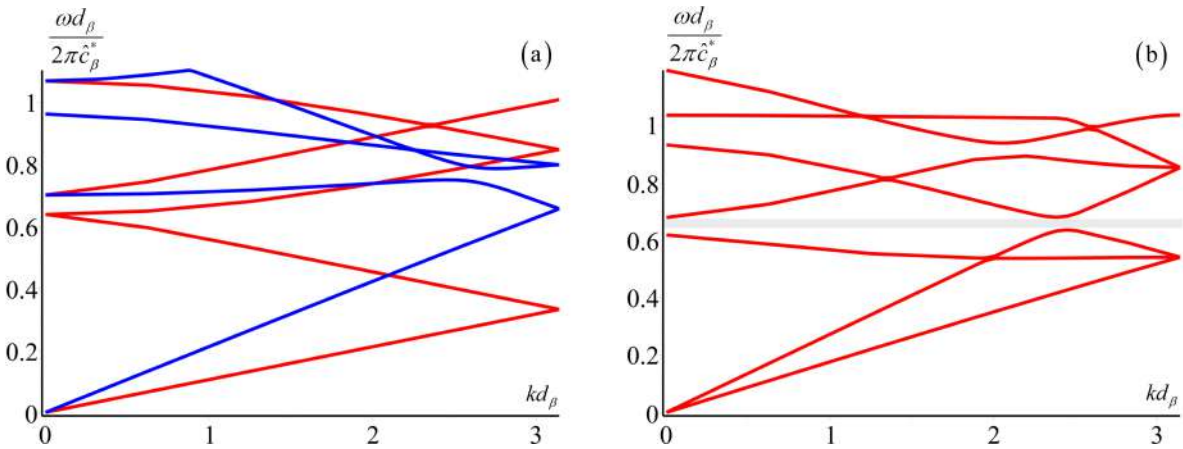

Figure 17: $E_m/E_i = 1 \cdot 10^{-1}$ and $E_r/E_m = 1$. Dispersion curves in the Brillouin zone.(a) waves in $\mathbf{e}_1$ and $\mathbf{e}_2$ directions: shear waves (red) and compressional waves (blue); (b)waves in $\mathbf{a}_3$ direction. The band gap is highlighted with the gray rectangle.

examined $(E_m/E_i = 0,\ E_m/E_i = 1 \cdot 10^{-2}$ and $E_m/E_i = 1 \cdot 10^{-1})$ in terms of dispersion curves in the Brillouin zone for waves propagating in the $\mathbf{a}_3$ direction and represented in Figures 11(b), 15(b) and 17(b), respectively. It results that, as E_m/E_i increases, a two-fold trend is recognized: the band gap is found for higher values of the angular frequency and its band width tends to decrease.
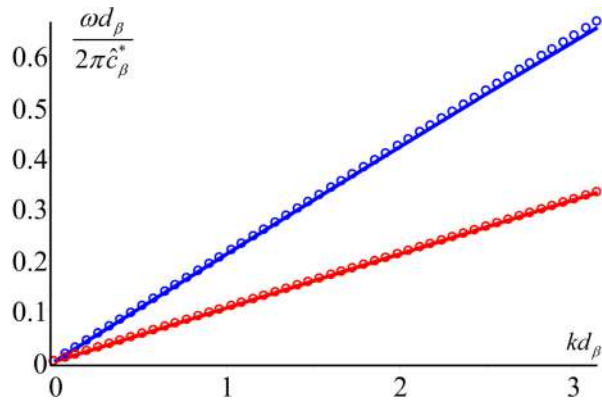
Figure 18: $E_m/E_i = 1 \cdot 10^{-1}$ and $E_r/E_m = 1$. Shear (red) and compressional (blue) dispersion curves along the orthotropic axes. Comparison between the Floquet-Bloch approach (solid lines) and the first order computational homogenization theory (dotted lines).

These circumstances suggest that, also in the dynamic response, the presence of the matrix and its properties, compared to the properties of the ligaments, strongly affect the global behavior of the anti-tetrachiral cellular solid. Therefore, a rational design of such a material cannot neglect these features.

Finally, in order to highlight further qualitative aspects of the studied class of microstructures, it seems useful to relate the auxetic character of the material with the existence of band gaps. By comparing the curves in Figure 8(c) with the plots in Figures 11, 15 and 17, it appears that maximum auxeticity occurs along the orthotropic axis of the materials ($\vartheta = \kappa\pi/2$, $\kappa = 0,1,2...$), while the full band gaps arise for waves propagating in $\mathbf{a}_3$ direction, that is for $\vartheta = \pi/4$. Moreover, the presence of the matrix material seems to have the dual effect of reducing both the auxeticity and the width of band gaps.

5. Final Remarks

The characterization of the novel class of anti-tetrachiral cellular solids has been tackled, both investigating the static and the dynamic response.

First the first order homogenized constitutive response has been investigated in static modeling. Two different models have been considered at the microscopic scale: a beam lattice model (Section 3.1), where the actual solid has been replaced by a discrete system of interconnected beams and the presence of the matrix has been neglected, and a continuous model in which the overall constitutive response has been evaluated adopting the first order computational homogenization technique.

In the case where no matrix filling the gaps between ligaments is considered, the comparison of the results obtained with the two models has been carried out. It has been emphasized that, despite

31

the strong simplifying assumptions of the beam lattice model, this approach gives reasonable results, comparable with those of the richer model, at least when the matrix is neglected. Both models are able to satisfactorily reproduce the experimental results reported in (Alderson et al., 2010), especially concerning the accurate estimation of the Poisson's ratio.

Besides, a direct comparison, in terms of elastic moduli, between the anti-tetrachiral and the tetra-chiral geometry suggests that the anti-tetrachiral cellular solid shows more a pronounced auxeticity, at least for the set of geometrical and material properties chosen in the example.

A further parametric study has been performed via the first order computational homogenization technique. The influence of mechanical and geometric parameters of the Periodic Cell on the 2D overall elastic moduli has been, indeed, investigated.

First, the influence of the ratio L/R between the distance and the radius of rings is considered. It can be noted from the plot of E_{hom} and ν_{hom} versus θ that below a certain value of L/R (namely $L/R=8$) the response is strongly affected by the geometric parameter, while above it is basically independent on L/R. Moreover, it emerges that the auxeticity of the material by the presence of the matrix between the ligaments. It results, indeed, that the case with $E_m/E_i = 0$ is characterized by the most pronounced auxeticity, for a fixed geometry of the cellular solid. In the other cases, in which a matrix between the ligaments is accounted for, a clear decrease of such property is detected as E_m/E_i increases, up to the a given ratio E_m/E_i beyond which the material loses its auxeticity properties.

Furthermore, the influence of the Young's modulus of the material possibly filling the rings (E_r) is analyzed. Although very low differences are found between the two considered cases ($E_r/E_i=10^{-3}$ and $E_r/E_i=1$), a rigid ring seems to increase the auxeticity of the material. The last part of the paper is devoted to the dynamic modeling and a further numerical investigation is performed on the flexural wave propagation properties. Also in this case two approaches are considered: a Floquet–Bloch wave approach and the first order computational homogenization are applied to the periodic cell of the cellular solid to evaluate the dispersion characteristics and phase constant surfaces as the geometric parameters of the periodic cell vary.

The analysis of the results in terms of dispersion curves in the Brillouin zone, examined in the dimensionless space, suggest that, also in the dynamic response, the presence of the matrix and its properties, compared to the properties of the ligaments, qualitatively influence the the global behavior of the anti-tetrachiral cellular solid. A two-fold trend is, indeed, recognized: the full band gap is found for higher values of the angular frequency and its band width tends to decrease.

32

It is noteworthy that the derivation of the analytical solution for the spectral band gaps can give useful information for the design of new complex auxetic materials which behave like elastic wave filters.

It also can be remarked that the first order homogenization theory, describing non-dispersive waves characterized by a a linear dependence between angular frequency and wave number, is able to satisfactorily reproduce the acoustic branch of the Bloch spectrum for a wide range of wavelengths. Finally, relating the auxetic character of the material with the existence of band gaps, it is possible to highlight further qualitative aspects of the studied class of microstructures. It emerges, in fact, that maximum auxeticity occurs along the orthotropic axis of the materials ($\vartheta = \kappa\pi/2$, κ=0,1,2...), while the full band gaps arise for waves propagating in $\mathbf{a}_3$ direction, that is for $\vartheta = \pi/4$. Moreover, the presence of the matrix material seems to have the dual effect of reducing the auxeticity and the width of band gaps.

Appendix A

In what follows, the same matrix representation as in (Addessi et al., 2014), is chosen. For the generic element represented in Figure 4, the displacements of the end nodes h and k are expressed in the basic local reference system by the following vector:

$$\mathbf{v}^{el} = \{v_1^h \; v_2^h \; \phi_h \; v_1^k \; v_2^k \; \phi_k\}^T \tag{38}$$

while in the global reference system, as:

$$\bar{\mathbf{w}}^{el} = \{\bar{u}_1^h \; \bar{u}_2^h \; \bar{\phi}_h \; \bar{u}_1^{\,k} \; \bar{u}_2^k \; \bar{\phi}_k\}^T \tag{39}$$

and the relation between them is the orthogonal rotation matrix $\mathbf{R}^{el}$, that is:

$$\mathbf{v}^{el} = \mathbf{R}^{el}\bar{\mathbf{w}}^{el} \quad \text{with} \quad \mathbf{R}^{el} = \begin{bmatrix} \cos\vartheta & \sin\vartheta & 0 & 0 & 0 & 0 \\ -\sin\vartheta & \cos\vartheta & 0 & 0 & 0 & 0 \\ 0 & 0 & 1 & 0 & 0 & 0 \\ 0 & 0 & 0 & \cos\vartheta & \sin\vartheta & 0 \\ 0 & 0 & 0 & -\sin\vartheta & \cos\vartheta & 0 \\ 0 & 0 & 0 & 0 & 0 & 1 \end{bmatrix} \tag{40}$$

The resulting strain components are an axial elongation δ and two nodal deformational rotations χ_h and χ_k (in the case of a simple supported beam chosen as fictitious isostatic system):

$$\boldsymbol{\varepsilon}^{el} = \{\delta \; \chi_h \; \chi_k\}^T \tag{41}$$

33

The compatibility equations results as:

$$\boldsymbol{\varepsilon}^{el} = \mathbf{D}^{el}\mathbf{v}^{el} \tag{42}$$

where the matrix $\mathbf{D}^{el}$ is:

$$\mathbf{D}^{el} = \begin{bmatrix} -1 & 0 & 0 & 1 & 0 & 0 \\ 0 & 1/L_{el} & 1 & 0 & -1/L_{el} & 0 \\ 0 & 1/L_{el} & 0 & 0 & -1/L_{el} & 1 \end{bmatrix} \tag{43}$$

where L_{el} is the length of the beam element. The stress components work conjugated with $\boldsymbol{\varepsilon}^{el}$ are:

$$\boldsymbol{\sigma}^{el} = \{N \ M_h \ M_k\}^T \tag{44}$$

and the equilibrium equations relating the resulting stresses with the vector of the internal forces $\mathbf{P}_I^{el}$ are:

$$\mathbf{D}^{elT}\boldsymbol{\sigma}^{el} = -\mathbf{P}_I^{el} \tag{45}$$

Linear elastic behavior is assumed as:

$$\boldsymbol{\sigma}^{el} = \mathbf{E}^{el}\boldsymbol{\varepsilon}^{el} \tag{46}$$

where

$$\mathbf{E}^{el} = \begin{bmatrix} EA_{el}/L_{el} & 0 & 0 \\ 0 & 4EJ_{el}/L_{el} & 2EJ_{el}/L_{el} \\ 0 & 2EJ_{el}/L_{el} & 4EJ_{el}/L_{el} \end{bmatrix} \tag{47}$$

being E the Young's modulus, A_{el} the area of the transversal section of the element and J_{el} the momentum of inertia. The element stiffness matrix expressed in the basic global reference system is:

$$\mathbf{k}^{el} = \mathbf{R}^{elT}\mathbf{D}^{elT}\mathbf{E}^{el}\mathbf{D}^{el}\mathbf{R}^{el} \tag{48}$$

and the nodal force vector at the end nodes of the generic beam element results as:

$$\bar{\mathbf{b}}^{el} = \mathbf{R}^{elT}\mathbf{P}_I^{el} \tag{49}$$

Rigid offset aligned with the global reference system are considered to account for the rigid crosses, see Figure 19.

By denoting with $\mathbf{f}^{el}$ the nodal force vector at the end nodes of the rigid offsets, the following relation holds:

$$\mathbf{b}^{el} = \mathbf{B}^T\bar{\mathbf{b}}^{el} \tag{50}$$

where

$$\mathbf{B}^T = \begin{bmatrix} \mathbf{B}_h^T & \mathbf{0} \\ \mathbf{0} & \mathbf{B}_k^T \end{bmatrix} \tag{51}$$
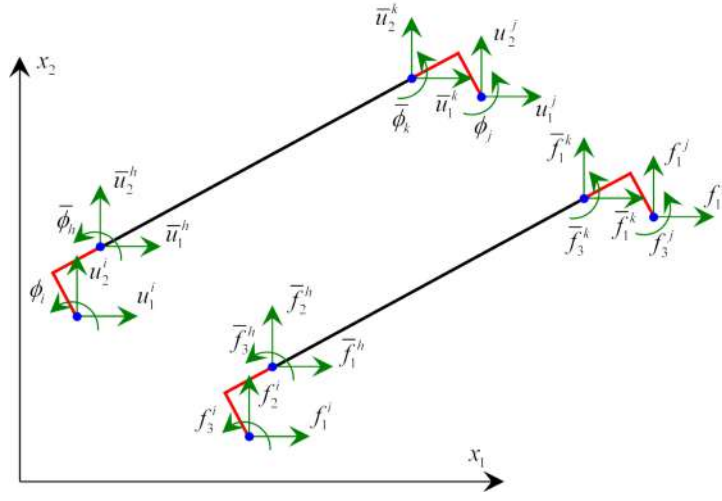
34

Figure 19: Rigid offset to account for rings in the anti-tetrachiral lattice.

with

$$
\mathbf{B}_h^T = \begin{bmatrix} 1 & 0 & 0 \\ 0 & 1 & 0 \\ -l_{y2h} & l_{y1h} & 1 \end{bmatrix}, \qquad \mathbf{B}_k^T = \begin{bmatrix} 1 & 0 & 0 \\ 0 & 1 & 0 \\ -l_{y2k} & l_{y1k} & 1 \end{bmatrix} \tag{52}
$$

and $\mathbf{0}$ denotes the 3×3 null matrix; $l_{y1h(k)}$ and $l_{y2h(k)}$ represent the rigid offset lengths at the end $h(k)$ parallel and orthogonal to the beam axis, respectively. These lengths are equal to the radius R of the ring of the anti-tetrachiral cellular solid, see Figure 2.

By exploiting the virtual work equivalence, the transformation rule between the nodal displacement degrees of freedom defined at the end nodes of the beam $\bar{\mathbf{u}}^{el}$ and at the end nodes of the rigid offsets $\mathbf{u}^{el}$ (in the global reference frame) are deduced as:

$$
\bar{\mathbf{w}}^{el} = \mathbf{B}\mathbf{w}^{el} \tag{53}
$$

Thus, the overall element stiffness matrix, accounting for the effect of the rigid offset, is:

$$
\mathbf{K}^{el} = \mathbf{B}^{elT}\mathbf{k}^{el}\mathbf{B}^{el} \tag{54}
$$

References

Addessi, D., De Bellis, M. L., Sacco, E., 2013. Micromechanical analysis of heterogeneous materials subjected to overall cosserat strains. Mech Res Commun 54, 27–34.

Addessi, D., Mastrandrea, A., Sacco, E., 2014. An equilibrated macro-element for nonlinear analysis of masonry structures. Engineering Structures 70 (0), 82 – 93.

Alderson, A., Alderson, K., Attard, D., Evans, K., Gatt, R., Grima, J., Miller, W., Ravirala, N., Smith, C., Zied, K., Jul. 2010. Elastic constants of 3-, 4- and 6-connected chiral and anti-chiral honeycombs subject to uniaxial in-plane loading. Composites Science and Technology 70 (7), 1042–1048.

Bacca, M., Bigoni, D., Dal Corso, F., Veber, D., 2013a. Mindlin second-gradient elastic properties from dilute two-phase Cauchy-elastic composites. Part I: Closed form expression for the effective higher-order constitutive tensor. Int. J. of Solids and Structures 50, 4010–4019.

Bacca, M., Bigoni, D., Dal Corso, F., Veber, D., 2013b. Mindlin second-gradient elastic properties from dilute two-phase Cauchy-elastic composites Part II: Higher-order constitutive properties and application cases. Int. J. of Solids and Structures 50, 4020–4029.

Bacigalupo, A., 2014. Second-order homogenization of periodic materials based on asymptotic approximation of the strain energy: formulation and validity limits. Meccanica 49 (6), 1407–1425.

Bacigalupo, A., Gambarotta, L., 2010. Second-order computational homogenization of heterogeneous materials with periodic microstructure. ZAMM Z. Angew. Math. Mech 90 (10-11), 796–811.

Bacigalupo, A., Gambarotta, L., 2013. A multi-scale strain-localization analysis of a layered strip with debonding interfaces. International Journal of Solids and Structures 50 (13), 2061–2077.

Bacigalupo, A., Gambarotta, L., 2014a. Homogenization of periodic hexa- and tetrachiral cellular solids. Composite Structures 116, 461–476.

Bacigalupo, A., Gambarotta, L., 2014b. Second-gradient homogenization model for wave propagation in heterogeneous periodic media. International Journal of Solids and Structures 51, 1052–1065.

Bettini, P., Airoldi, A., Sala, G., Landro, L. D., Ruzzene, M., Spadoni, A., 2010. Composite chiral structures for morphing airfoils: Numerical analyses and development of a manufacturing process. Composites Part B: Engineering 41 (2), 133–147.

36

Brillouin, L., 1946. Wave propagation in periodic structures: electric filters and crystal lattices. "Int. series in pure and applied physics". McGraw-Hill, New York.

Cadman, J. E., Zhou, S., Chen, Y., Li, Q., 2013. On design of multi-functional microstructural materials. J. Material Science 48, 51–66.

Cauchi, J., Grima, J., 2014. Modelling of the static and dynamic properties of tho-type silicates. TASK Quarterly Journal 18, 5–65.

Chen, Y., Scarpa, F., Liu, Y., Leng, J., 2013. Elasticity of anti-tetrachiral anisotropic lattices. International Journal of Solids and Structures 50 (6), 996–1004.

De Bellis, M., Addessi, D., 2011. A Cosserat based multi-scale model for masonry structures. Int J Multiscale Com 9 (5), 543–563.

Dirrenberger, J., Forest, S., Jeulin, D., 2012. Elastoplasticity of auxetic materials. Computational Material Science 64, 57–61.

Dirrenberger, J., Forest, S., Jeulin, D., 2013. Effective elastic properties of auxetic microstructures: anisotropy and structural applications. International Journal of Mechanics and Materials in Design 9 (1), 21–33.

Dirrenberger, J., Forest, S., Jeulin, D., Colin, C., 2011. Homogenization of periodic auxetic materials. Procedia Engineering 10, 1847–1852.

Dos Reis, F., Ganghoffer, J., Dec. 2012. Construction of micropolar continua from the asymptotic homogenization of beam lattices. Computers & Structures 112-113, 354–363.
URL http://linkinghub.elsevier.com/retrieve/pii/S0045794912001940

Forest, S., 2002. Homogenization methods and the mechanics of generalized continua - part 2. Theoretical and applied mechanics 28-29, 113–143.

Forest, S., Sab, K., 1998. Cosserat overall modeling of heterogeneous materials. Mech Res Commun 25, 449–454.

Gaspar, N., Ren, X., Smith, C., Grima, J., Evans, K., 2005. Novel honeycombs with auxetic behaviour. Acta Materialia 53 (8), 2439–2445.

Gatt, R., Attard, D., Farrugia, P., Azzopardi, K., Mizzi, L., Brincat, J., Grima, J., 2013. A realistic generic model for anti-tetrachiral systems. Physica Status Solidi (b) 250, 2012–2019.

Ghosh, S., Lee, K., Moorthy, S., 1996. Two scale analysis of heterogeneous elastic plastic materials with asymptotic homogenisation and voronoi cell finite element model. Computer Methods in Applied Mechanics & Engineering 132, 63–116.

Greaves, G., Greer, A., Lakes, R., Rouxel, T., 2011. Poissons ratio and modern materials. Nature Materials 10, 823–837.

Grima, J. N., Gatt, R., Ferrugia, P. S., 2008. On the Properties of Auxetic Meta-Tetrachiral Structures . Phys Status Solidi B 245 (3), 511–520.

Guedes, J., Kikuchi, N., 1990. Preprocessing and postprocessing for materials based on the homogeneization method with adaptative finite element method. Computer Methods in Applied Mechanics & Engineering 83, 143–198.

Kouznetsova, V., Geers, M., Brekelmans, W., 2004. Multi-scale second-order computational homogenization of multi-phase materials: a nested finite element solution strategy. Comput Method Appl M 193, 5525–5550.

Lakes, R., 1987. Foam structures with a negative Poisson's ratio. Science 235, 1038–1040.

Lakes, R., 1991. Deformation mechanisms of negative Poisson's ratio materials: structural aspects. J. Mater. Sci. 26, 2287–2292.

Lakes, R., 1993. Materials with structural hierarchy. Nature 361, 511–515.

Ma, Y., Scarpa, F., Zhang, D., Zhu, B., Chen, L., Hong, J., 2013. A nonlinear auxetic structural vibration damper with metal rubber particles. Smart Materials and Structures 22, 084012.

Miehe, C., 2002. Strain-driven homogenization of inelastic microstructures andcomposites based on an incremental variational formulation. Int J Numer Meth Eng 55, 1285–1322.

Nemat-Nasser, S., Willis, Srivastava, A., Amirkhizi, A., 2011. Homogenization of periodic elastic composites and locally resonant sonic materials. Phys. Rev. B. 83, 104103.

Prall, D., Lakes, R., 1996. Properties of a chiral honeycomb with a Poisson's ratio of -1. Int J Mech Sci 39, 305–314.

Prawoto, Y., 2012. Seeing auxetic materials from the mechanics point of view : A structural review on the negative Poisson's ratio. Computational Materials Science 58, 140–153.

Scarpa, F., Blain, S., Lew, T., Perrott, D., Ruzzene, M., Yates, J., 2007. Elastic buckling of hexagonal chiral cell honeycombs. Compos A Appl Sci Manuf 38, 280–289.

Schenk, M., Guest, S., 2013. Geometry of Miura-folded metamaterials. PNAS 110, 3276–3281.

Sigmund, O., Torquato, S., Aksay, I. A., 1998. On the design of 1-3 piezocomposites using topology optimization. J.Mater. Res. 13, 1038 –1048.

Smith, C., Grima, J., Evans, K., 2000. A novel mechanism for generating auxetic behaviour in reticulated foams: missing rib foam model. Acta Materialia 48, 4349–4356.

Spadoni, A., Ruzzene, M., Gonella, S., Scarpa, F., 2009. Phononic properties of hexagonal chiral lattices. Wave Motion 132, 435–450.

Tee, K. F., Spadoni, a., Scarpa, F., Ruzzene, M., 2010. Wave Propagation in Auxetic Tetrachiral Honeycombs. Journal of Vibration and Acoustics 132 (3), 0310071–8.

Trovalusci, P., Capecchi, D., Ruta, G., 2009. Genesis of the multiscale approach for materials with microstructrues. Archive of Applied Mechanics 79, 981–997.